Variational modeling of hydromechanical fracture in saturated porous media: a micromechanics-based phase-field approach[☆,☆☆]

Jacinto Ulloa[a,b], Nima Noii[c], Roberto Alessi[d], Fadi Aldakheel[c,e], Geert Degrande[a], Stijn François[a]

[a] *Department of Civil Engineering, KU Leuven, Kasteelpark Arenberg 40, B-3001 Leuven, Belgium*
[b] *Division of Engineering and Applied Science, California Institute of Technology, Pasadena, CA 91125, USA*
[c] *Institute of Continuum Mechanics, Leibniz Universität Hannover, An der Universität 1, 30823 Garbsen, Germany*
[d] *Department of Civil and Industrial Engineering, Università di Pisa, Largo Lucio Lazzarino 2, 56122 Pisa, Italy*
[e] *Zienkiewicz Centre for Computational Engineering, Faculty of Science and Engineering, Swansea University, Bay Campus, SA1 8EN Swansea, UK*

Abstract

This paper presents a novel variational phase-field model for different fracture processes in fully saturated porous media. As a key feature, the model employs a micromechanics-based theory for the description of brittle-tensile and compressive-ductile fracture. As such, the field variables are linked to physical mechanisms at the microcrack level, with damage emerging as the consequence of microcrack growth. Similarly, plasticity emerges as a consequence of the frictional sliding of closed microcracks. In this way, the evolution of opening microcracks in tension leads to (mode I) brittle fracture, while the evolution of closed microcracks in compression/shear leads to (mode II) ductile fracture. These failure mechanisms are coupled to fluid flow, resulting in a Darcy-Biot–type hydromechanical model. Therein, in the tensile regime, plasticity naturally vanishes, while damage is driven by poroelastic energy, accounting for the pressure in fluid-filled opening microcracks. On the other hand, in the compressive/shear regime, the plastic driving force naturally follows as a Terzaghi-type effective stress in terms of the local stress field acting on the microcrack surfaces, while damage is solely driven by the frictionally blocked free energy. As another important feature, the model includes a non-associative frictional plasticity law. Nevertheless, a thermodynamically consistent variational framework is employed, for which different energetic principles are discussed. Finally, the numerical simulations show that the model captures relevant hydromechanical coupling effects in benchmark problems, including mechanically induced shear fracture and hydraulically induced tensile fracture.

Keywords: Phase-field models; Micromechanics; Hydraulic fracture; Porous media; Variational formulation; Non-associative plasticity

[☆] *Postprint version.*
[☆☆] *Published version:* J. Ulloa, N. Noii, R. Alessi, F. Aldakheel, G. Degrande, and S. François. Variational modeling of hydromechanical fracture in saturated porous media: a micromechanics-based phase-field approach. *Computer Methods in Applied Mechanics and Engineering*, 396:115084, 2022.
DOI: `https://doi.org/10.1016/j.cma.2022.115084`

*Corresponding author: Jacinto Ulloa, Fadi Aldakheel
Email addresses: `julloa@caltech.edu` (Jacinto Ulloa), `noii@ikm.uni-hannover.de` (Nima Noii), `roberto.alessi@unipi.it` (Roberto Alessi), `aldakheel@ikm.uni-hannover.de` (Fadi Aldakheel), `geert.degrande@kuleuven.be` (Geert Degrande), `stijn.francois@kuleuven.be` (Stijn François)

Contents

1. Introduction

Quasi-brittle geomaterials such as rocks and concrete are subject to variations in pore pressure as fluid flows through their porous microstructure. This mechanism and its interplay with mechanical deformation involve porosity changes that alter the material's structural properties. Consequently, the evolution of porosity is considered to be the key for understanding and predicting the behavior of porous media, including transport properties, strength, and fracture [1]. The study of these phenomena is crucial to assess the strength of materials under fully or partially water-saturated conditions, as encountered, for instance, in offshore structures, whose load-bearing capacity is strongly influenced by pore pressure [2]. Moreover, fluid-related fracture processes are crucial in several engineering applications such as tunnel excavation, nuclear waste storage, and hydraulic fracture for oil and gas extraction or the stimulation of geothermal reservoirs. Assessing the applicability and the risk associated with such practices calls for a deep understanding of the coupled hydromechanical behavior of geomaterials, particularly under failure conditions.

The dissipative behavior of quasi-brittle geomaterials is modulated by the evolution of microcracks in the solid skeleton. Depending on the stress state and the kinematics at the microcrack level, different macroscopic behaviors are observed: brittle behavior in a tensile regime, associated with opening microcracks, and ductile behavior in a compressive/shear regime, associated with the frictional sliding of closed microcracks. Phenomenological damage and plasticity models in the context of geomaterials characterize such responses using internal variables defined at the continuum scale. While successful models of this type have been proposed [3–9], they often lack physical meaning and involve a large number of parameters. Some constitutive models [10, 11] overcome these shortcomings, presenting close links to the micromechanical description of damage and (friction-induced) plasticity in microcracked quasi-brittle materials [12–17]. In these latter works, coupling between microcrack growth and frictional sliding is considered to derive constitutive equations via suitable homogenization schemes, endowing the model with a clear physical meaning.

The studies above deal with dry materials or monophasic solids. Conversely, extensions of both phenomenological and micromechanics-based plastic-damage models have been proposed to consider the effect of pore pressure [18–24], usually in line with Biot's macroscopic theory for porous media [25]. We refer the reader to Coussy [26] for a thorough account of poroelasticity and poroplasticity and to Dormieux et al. [1] for a treatment based on micromechanics. For the purposes of the present study, we highlight the work of Xie et al. [23], where the micromechanics approach to damage and frictional plasticity [15] was extended to porous media in fluid-saturated conditions. This topic was further studied in Jia et al. [24].

The plastic-damage models discussed so far are based on local internal variables and are thus unable to handle softening responses with strain localization, where the well known loss of ellipticity leads to pathological mesh-dependence and vanishing energy dissipation in finite element simulations. Remarkably, similar issues have been reported in non-associative plasticity models [27, 28], despite their widespread application to geomaterials. Thus, a delicate treatment of localized responses is required to model failure in geomaterials. Different techniques for this purpose can be roughly divided into (i) models with sharp discontinuities and (ii) models with regularized kinematics. The first class involves, for instance, the use of strong discontinuities [29–31], as recently considered in a micromechanics-based plastic-damage model for quasi-brittle materials [32]. Strong discontinuities have also been applied in phenomenological poroplasticity models to capture shear bands in fluid-saturated materials [33–36]. A similar approach was recently employed in a discrete beam lattice model [37, 38]. On the other hand, the second family of models includes rate-dependent [39, 40], Cosserat [41, 42], non-local [43–45], and gradient-enhanced [46–48] theories. Most of these works focus on material softening, although recent attention has also been placed on non-associative plasticity [28, 49, 50]. As in the case of sharp discontinuities, regularized models have also been applied to describe hydromechanical failure in porous media [51–53]. A comparative overview of techniques belonging to the two mentioned classes in the context of hydraulic fracture can be found in Yoshioka et al. [54].

Of special interest for the present work is the phase-field approach to fracture, a topic that has gained significant attention in the past decade. Phase-field models have shown great ability to describe crack initiation, propagation, branching, and merging, providing a powerful paradigm in computational fracture mechanics. Starting with the variational formulation of Griffith's fracture [55] and its subsequent regularization [56], the phase-field approach has become widely accepted in the mechanics community as a specific case of gradient damage [57–65]. Several modifications of the original theory have been proposed, for instance, to account for tension/compression asymmetry using energy splits, either in a variational form [57, 58, 66–68] or by abandoning the variational structure of the original theory [69, 70]. Tension/compression asymmetry has also been incorporated without resorting to energy splits [71], albeit in a non-variational form.

Despite this progress, most phase-field models cannot describe the peculiar fracture behavior of geomaterials. For instance, in rock-like materials, the critical energy release rate for mode I (tensile) fracture is significantly lower than the critical energy release rate for mode II (shear) fracture [72]. Moreover, the fracture mode is strongly pressure-dependent (in the sense of confining stress), exhibiting a brittle-to-ductile transition with increasing confinement [73]. Several variations of phase-field models have been proposed to address these problems. Initial efforts focused on shear fracture [74], while subsequent works [75–77] considered mixed-mode fracture, mostly inspired by the so-called F-criterion [72]. Other studies have taken pressure-dependent frictional behavior into account [78], as well as plastic coupling [79–82]. More recently, a micromechanics-based approach to fracture in geomaterials was proposed [83, 84], where the macroscopic crack phase-field and the plastic strain tensor are linked to mechanisms at the microcrack level. In addition to preserving variational consistency, this approach provides a physically meaningful description of tensile-brittle and compressive-ductile behavior, without employing heuristic energy splits.

All phase-field models discussed so far focus on monophasic materials. However, phase-field models have also been extended to fluid-driven fracture in porous media [85–95] (see Heider [96] and Wick [97] for overviews). Therein, Darcy's law is usually employed as a phenomenological assumption to model fluid flow through the unbroken porous material, governed by the pressure (or chemical potential) gradient. On the other hand, a different law is employed to describe fluid flow in fully developed cracks. For instance, assuming small crack openings, a Poiseuille-type flow is considered in some studies [95, 98–101]. Then, an evolving anisotropic permeability tensor is introduced, represented by a deformation-dependent function scaled by the crack opening and coupled to damage evolution. Only a few recent works [2, 102, 103] have extended this approach to ductile behavior. Therein, a phenomenological Drucker-Prager plasticity model is considered.

The purpose of the present work is to introduce a new hydromechanical coupled model able to describe the main features of geomaterial failure in fluid-saturated conditions, including both brittle and ductile behavior. In contrast with purely phenomenological models, we take the micromechanics-based phase-field approach to tensile-brittle and compressive-ductile fracture, recently proposed by Ulloa et al. [83], as a point of departure, and extend the formulation to hydromechanical coupling under saturated conditions. The resulting model can thus be viewed as a multiphysics extension of the model presented in Ulloa et al. [83].

Concerning the constitutive behavior, we highlight the following features of the present study: the micromechanical root of field variables, material parameters, and constitutive relations, endowing the model with a clear physical interpretation; an asymmetric behavior in tension and compression that does not require the heuristic energy splits typically considered in phase-field models; a natural distinction between mode I (tensile-brittle) and mode II (compressive-ductile) fracture regimes; and the use of a non-associative frictional plasticity law, allowing for a realistic description of the dissipative behavior of geomaterials. These mechanisms are hereby coupled to fluid transport, for which the permeability tensor entails a transition from Darcy flow to Poiseuille flow between intact and fully broken material points. For this purpose, the standard approach set forth by Miehe and Mauthe [95] and related works [98, 100, 103] is adopted, although different techniques could also be employed without altering the novel aspects of the model.[1]

From the perspective of the formulation, the main feature of this study is a rigorous and thermodynamically consistent variational framework. To this end, we employ the principles of the energetic formulation [104], namely, energy balance and stability, considering a combination between rate-independent

[1] As reported in the literature, the specific approach adopted to modify the permeability tensor at fracture presents certain limitations, to be discussed in the sequel, for which we do not intend to provide a solution. Instead, the focus of this work lies in the variational micromechanics-based treatment of damage and plasticity and its coupling to fluid flow.

dissipative processes and the rate-dependent process of fluid transport. The non-associative evolution law is carefully incorporated in the variational framework using a state-dependent dissipation potential and a generalization of the principle of maximum dissipation [105]. The developed formulation is linked to compact rate-type minimization and saddle-point variational principles.

The paper is structured as follows. Section 2 presents the general modeling framework and introduces variational principles for porous solids with gradient-extended internal variables coupled to fluid flow. These concepts are used to construct the proposed micromechanics-based phase-field model in section 3, starting with a brief description of the micromechanical background. The numerical implementation is discussed in section 4, while numerical simulations that highlight the main features of the model are presented in section 5. Concluding remarks are finally drawn in section 6.

2. Variational framework for porous media with gradient-extended internal variables

The purpose of this section is to introduce a general variational framework for gradient-extended dissipative solids coupled to fluid flow. We begin by presenting the problem outline and some classical definitions in sections 2.1–2.3. Then, section 2.4 establishes the evolution problem in terms of the energetic formulation, where, following Mielke and Roubícek [104], an extension to rate-dependent phenomena is considered to incorporate the fluid transport equations. In section 2.5, this formulation is linked to compact rate-type minimization and saddle-point principles, in agreement with Miehe et al. [106, 107] and related works.

2.1. Problem outline

Consider a deformable porous solid in a fixed reference domain $\Omega \subset \mathbb{R}^3$ with boundary Γ (figure 1). The goal is to describe the evolution of the porous medium due to hydromechanical actions. The deformation process is assumed to be quasi-static, occurring in a time interval $\mathrm{T} := [0, t_{\max}]$, where strain localization and fracture may develop. Concerning mechanical loads, the boundary is split into a Dirichlet part Γ^u_{D} with prescribed displacements $\bar{\boldsymbol{u}}(\boldsymbol{x}, t) \in \mathbb{R}^3$ and a Neumann part Γ^u_{N} with prescribed tractions $\bar{\boldsymbol{t}}(\boldsymbol{x}, t) \in \mathbb{R}^3$, where $\Gamma^u_{\mathrm{D}} \cup \Gamma^u_{\mathrm{N}} = \Gamma$ and $\Gamma^u_{\mathrm{D}} \cap \Gamma^u_{\mathrm{N}} = \varnothing$. The solid may also be subjected to body forces per unit mass $\boldsymbol{b}(\boldsymbol{x}, t) \in \mathbb{R}^3$. Fluid-driven external actions are considered at the boundary by means of a prescribed flux $\bar{h}(\boldsymbol{x}, t) \in \mathbb{R}$ on Γ^p_{N} and a prescribed pore pressure $\bar{p}(\boldsymbol{x}, t) \in \mathbb{R}$ on Γ^p_{D}, where $\Gamma^p_{\mathrm{D}} \cup \Gamma^p_{\mathrm{N}} = \Gamma$ and $\Gamma^p_{\mathrm{D}} \cap \Gamma^p_{\mathrm{N}} = \varnothing$. For the sake of simplicity, the effect of gravity on the fluid is neglected, and no internal fluid source in Ω is considered.

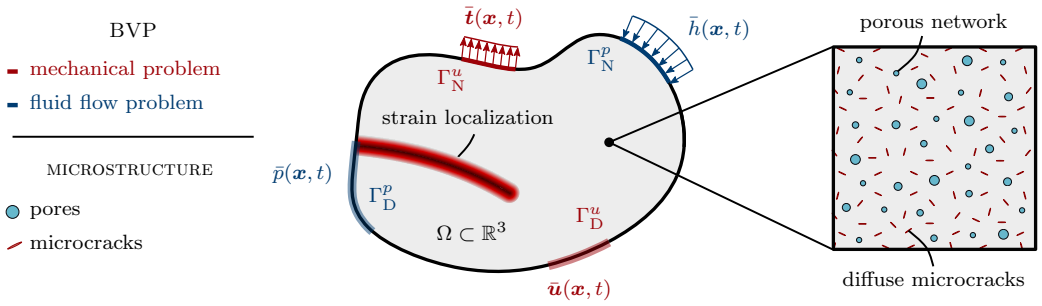

Fig. 1. Schematic representation of the multiphysics boundary value problem in a microcracked porous solid with a strain localization zone, representing, e.g., a smeared fracture.

The microstructure of the solid consists of a porous matrix embedded with microcracks, as depicted in figure 1. The microcrack mechanisms will be discussed in detail in section 3. On the other hand, Biot's macroscopic theory [25] is adopted to describe the porous medium under fully saturated conditions. As such,

the matrix material is permeated by an interconnected pore space, assumed to be either completely dry or completely filled with a viscous fluid. In the dry case, the effect of air is neglected and the material can be viewed as a monophasic solid. Conversely, the saturated matrix material is described at the continuum scale as a biphasic system, where each material point $\boldsymbol{x} \in \Omega$ corresponds to an elementary volume $\mathrm{d}\Omega = \mathrm{d}\Omega^{\mathrm{s}} + \mathrm{d}\Omega^{\mathrm{f}}$. Here, $\mathrm{d}\Omega^{\mathrm{s}}$ is the volume of the solid phase and $\mathrm{d}\Omega^{\mathrm{f}}$ is the volume of the fluid phase occupying the pore space. Then, the volume fractions ϑ^{s} and ϑ^{f} characterize the saturation condition

$$\vartheta^{\mathrm{s}} + \vartheta^{\mathrm{f}} = 1 \qquad \text{with} \qquad \vartheta^{\mathrm{s}} = \frac{\mathrm{d}\Omega^{\mathrm{s}}}{\mathrm{d}\Omega} \quad \text{and} \quad \vartheta^{\mathrm{f}} = \frac{\mathrm{d}\Omega^{\mathrm{f}}}{\mathrm{d}\Omega},$$

where ϑ^{f} is a (Lagrangian) porosity. The mixture density at each material point reads

$$\rho = \rho^{\mathrm{s}} + \rho^{\mathrm{f}} \quad \text{with partial densities} \quad \rho^{\mathrm{s}} = \vartheta^{\mathrm{s}} \rho^{\mathrm{s}}_{\mathrm{R}} \quad \text{and} \quad \rho^{\mathrm{f}} = \vartheta^{\mathrm{f}} \rho^{\mathrm{f}}_{\mathrm{R}},$$

where $\rho^{\mathrm{s}}_{\mathrm{R}} = m^{\mathrm{s}}/\mathrm{d}\Omega^{\mathrm{s}}$ and $\rho^{\mathrm{f}}_{\mathrm{R}} = m^{\mathrm{f}}/\mathrm{d}\Omega^{\mathrm{f}}$ are the mass densities of the solid phase and the fluid phase.

2.2. State variables and fundamental balance laws

The small strain hypothesis is assumed throughout this work. The displacement field $\boldsymbol{u}\colon \Omega \times \mathrm{T} \to \mathbb{R}^3$ is then taken as a primary variable, with the compatible strain tensor $\boldsymbol{\varepsilon}\colon \Omega \times \mathrm{T} \to \mathbb{R}^{3\times3}_{\mathrm{sym}} \coloneqq \{\boldsymbol{e} \in \mathbb{R}^{3\times3} \,|\, \boldsymbol{e} = \boldsymbol{e}^{\mathrm{T}}\}$ obeying the linear relation $\boldsymbol{\varepsilon} = \nabla^{\mathrm{s}}\boldsymbol{u}$. The fluid phase is characterized by the normalized *fluid content variation*

$$\zeta \coloneqq \frac{\rho^{\mathrm{f}} - \rho^{\mathrm{f}}_0}{\rho^{\mathrm{f}}_{\mathrm{R}0}} = \left(\frac{\rho^{\mathrm{f}}_{\mathrm{R}}}{\rho^{\mathrm{f}}_{\mathrm{R}0}}\right)\vartheta^{\mathrm{f}} - \vartheta^{\mathrm{f}}_0,$$

where the subscript 0 denotes an initial quantity, i.e., at $t = 0$. The evolution of ζ is associated with the pore pressure field $p\colon \Omega \times \mathrm{T} \to \mathbb{R}$; as will become clear in subsequent developments, the pressure field is conveniently considered as an independent variable in the formulation. For the sake of simplicity, we assume hereinafter that the fluid is incompressible, such that $\rho^{\mathrm{f}}_{\mathrm{R}} = \rho^{\mathrm{f}}_{\mathrm{R}0}$ remains constant and $\zeta = \vartheta^{\mathrm{f}} - \vartheta^{\mathrm{f}}_0$ at all times.

Concerning the dissipative behavior of the microcrack structure, i.e., the evolution of microcracks and their localization into macroscopic fractures, the framework of thermomechanics with gradient-enhanced internal variables is adopted in this work. In the general formulation presented in this section, this behavior is characterized by a generic set of internal variables $\mathbf{a}\colon \Omega \times \mathrm{T} \to \mathbb{R}^m$ and their first-order spatial gradients $\nabla\mathbf{a}\colon \Omega \times \mathrm{T} \to \mathbb{R}^{3m}$. The internal variables will take a specific form in the model proposed in section 3.

The evolution of the state variables above must comply with the fundamental laws of continuum mechanics. The first is the balance of linear momentum, enforced through the static admissibility of the Cauchy stress tensor $\boldsymbol{\sigma}\colon \Omega \times \mathrm{T} \to \mathbb{R}^{3\times3}_{\mathrm{sym}}$. This condition implies the equilibrium equations for all $t \in \mathrm{T}$:

$$\mathrm{div}\boldsymbol{\sigma} + \rho\boldsymbol{b} = \boldsymbol{0} \quad \text{in } \Omega \qquad \text{and} \qquad \boldsymbol{\sigma}\cdot\boldsymbol{n} = \bar{\boldsymbol{t}} \quad \text{on } \Gamma^u_{\mathrm{N}}, \qquad \text{with} \qquad \boldsymbol{u} = \bar{\boldsymbol{u}} \quad \text{on } \Gamma^u_{\mathrm{D}}, \tag{1}$$

where $\boldsymbol{n}$ is the outward normal unit vector. The second fundamental law is the balance of mass, which accounts for fluid diffusion in terms of the fluid flux vector $\boldsymbol{h}\colon \Omega \times \mathrm{T} \to \mathbb{R}^3$. The balance of mass is enforced for all $t \in \mathrm{T}$ by the fluid balance equations

$$\dot{\zeta} + \mathrm{div}\boldsymbol{h} = 0 \quad \text{in } \Omega \qquad \text{and} \qquad \boldsymbol{h}\cdot\boldsymbol{n} = \bar{h} \quad \text{on } \Gamma^p_{\mathrm{N}}, \qquad \text{with} \qquad p = \bar{p} \quad \text{on } \Gamma^p_{\mathrm{D}}. \tag{2}$$

At this point, constitutive equations are required to relate the primary fields to the quantities $\boldsymbol{\sigma}$ and $\boldsymbol{h}$ appearing in the balance laws (1) and (2). Moreover, additional evolution equations are required to describe

the evolution of the internal variables contained in $\mathbf{a}$. These missing ingredients are introduced below.

2.3. Thermomechanical framework: constitutive relations and evolution equations

In line with the theory of generalized standard materials [108], the evolution of the system is characterized by two basic energy quantities: an internal energy density and a dissipation potential. Concerning the former, we let $\psi \coloneqq \psi(\boldsymbol{\varepsilon}, \zeta, \mathbf{a}, \nabla\mathbf{a})$ denote a Helmholtz-type free energy density. The second law of thermodynamics is taken as an a priori restriction, given for isothermal processes by the Clausius-Duhem inequality

$$\delta \coloneqq \boldsymbol{\sigma} : \dot{\boldsymbol{\varepsilon}} + p\,\dot{\zeta} - \dot{\psi}(\boldsymbol{\varepsilon}, \zeta, \mathbf{a}, \nabla\mathbf{a}) - \boldsymbol{h} \cdot \nabla p \geq 0. \tag{3}$$

Due to the distinct nature of the dissipative processes, stronger conditions are generally employed to enforce the Clausius-Duhem inequality [109], where the *intrinsic dissipation* δ_{int} and the *convective dissipation* δ_{con} are enforced to be non-negative separately. In the present case, from inequality (3), one has

$$\delta_{\text{int}} = \boldsymbol{\sigma} : \dot{\boldsymbol{\varepsilon}} + p\,\dot{\zeta} - \dot{\psi}(\boldsymbol{\varepsilon}, \zeta, \mathbf{a}, \nabla\mathbf{a}) \geq 0, \tag{4}$$

$$\delta_{\text{con}} = -\boldsymbol{h} \cdot \nabla p \geq 0. \tag{5}$$

From the intrinsic dissipation inequality (4), the Coleman-Noll procedure yields the constitutive relations

$$\boldsymbol{\sigma} = \frac{\partial \psi}{\partial \boldsymbol{\varepsilon}}(\boldsymbol{\varepsilon}, \zeta, \mathbf{a}, \nabla\mathbf{a}) \qquad \text{and} \qquad p = \frac{\partial \psi}{\partial \zeta}(\boldsymbol{\varepsilon}, \zeta, \mathbf{a}, \nabla\mathbf{a}). \tag{6}$$

On the other hand, the generalized stresses conjugate to $\mathbf{a}$ read

$$\mathbf{s} = -\delta_{\mathbf{a}}\psi(\boldsymbol{\varepsilon}, \zeta, \mathbf{a}, \nabla\mathbf{a}), \tag{7}$$

where $\delta_{\diamond} \coloneqq \partial_{\diamond} - \text{div}[\partial_{\nabla\diamond}]$ denotes the spatial Euler-Lagrange operator. Using equations (6) and (7), and evaluating inequality (3) in integral form, the condition $\delta_{\text{int}} > 0$ yields

$$\mathbf{s} \cdot \dot{\mathbf{a}} \geq 0 \quad \text{in } \Omega \qquad \text{and} \qquad -\big(\boldsymbol{n} \cdot \partial_{\nabla\mathbf{a}}\psi(\boldsymbol{\varepsilon}, \zeta, \mathbf{a}, \nabla\mathbf{a})\big) \cdot \dot{\mathbf{a}} \geq 0 \quad \text{on } \Gamma. \tag{8}$$

For rate-independent systems, the dissipation rate δ_{int} is characterized by a thermodynamically admissible dissipation potential ϕ_{int}, i.e., a non-negative, convex 1-homogeneous function in $\{\dot{\mathbf{a}}, \nabla\dot{\mathbf{a}}\}$, non-differentiable and vanishing at null rates. Then, defining for notational simplicity the constitutive state as $\mathbf{c} \coloneqq \{\boldsymbol{\varepsilon}, \zeta, \mathbf{a}, \nabla\mathbf{a}\}$, we have

$$\delta_{\text{int}} \coloneqq \phi_{\text{int}}(\dot{\mathbf{a}}, \nabla\dot{\mathbf{a}}; \mathbf{c}, \mathbf{s}) \geq 0. \tag{9}$$

Following Ulloa et al. [105], the intrinsic dissipation potential depends on the generalized stresses $\mathbf{s}$ to account for non-associative flow; this aspect is key for the model presented in Ulloa et al. [83] as well as for the present extension to saturated porous media. From equations (7)–(9) the evolution equations for the internal variable set $\mathbf{a}$ follow as

$$\begin{aligned} \delta_{\mathbf{a}}\psi(\boldsymbol{\varepsilon}, \zeta, \mathbf{a}, \nabla\mathbf{a}) + \delta_{\dot{\mathbf{a}}}\phi_{\text{int}}(\dot{\mathbf{a}}, \nabla\dot{\mathbf{a}}; \mathbf{c}, \mathbf{s}) \ni \mathbf{0} \quad &\text{in } \Omega, \\ \boldsymbol{n} \cdot \big(\partial_{\nabla\mathbf{a}}\psi(\boldsymbol{\varepsilon}, \zeta, \mathbf{a}, \nabla\mathbf{a}) + \partial_{\nabla\dot{\mathbf{a}}}\phi_{\text{int}}(\dot{\mathbf{a}}, \nabla\dot{\mathbf{a}}; \mathbf{c}, \mathbf{s})\big) \ni \mathbf{0} \quad &\text{on } \Gamma. \end{aligned} \tag{10}$$

Here, in view of the non-differentiability of ϕ_{int}, the multivalued subdifferential $\partial_{\diamond}\square(\diamond)$ of a function $\square$ at $\diamond$ (embedded in the operator $\delta_{\diamond}\square(\diamond)$) is employed in the context of convex analysis (see, e.g., Francfort [110]).

Equation (10) represents the strong form of the evolution equations for gradient-extended internal variables, e.g., describing the evolution of the microcrack structure and the resulting strain localization in figure 1.

Finally, we proceed to evaluate the convective dissipation inequality (5). Similar to the intrinsic counterpart, we enforce the non-negativity of δ_{con} by means of a suitable dissipation potential ϕ_{con}, which in this case is a 2-homogeneous convex function of the flux $\boldsymbol{h}$. Specifically, we have

$$\delta_{\text{con}} \coloneqq \frac{\partial}{\partial \boldsymbol{h}} \phi_{\text{con}}(\boldsymbol{h}; \mathbf{c}) \cdot \boldsymbol{h} \geq 0. \tag{11}$$

For subsequent developments, it is convenient to define the Legendre transform

$$\phi_{\text{con}}(\boldsymbol{h}; \mathbf{c}) = \sup \left\{ \boldsymbol{q} \cdot \boldsymbol{h} - \phi^{\star}_{\text{con}}(\boldsymbol{q}; \mathbf{c}) \right\}, \quad \text{with} \quad \boldsymbol{q} \coloneqq -\nabla p, \tag{12}$$

where $\phi^{\star}_{\text{con}}$ is the *dual* convective dissipation potential, a convex 2-homogeneous function of the negative pressure gradient $\boldsymbol{q}$. Then, we obtain the relation between the flux and the pressure gradient as

$$\boldsymbol{h} = \frac{\partial}{\partial \boldsymbol{q}} \phi^{\star}_{\text{con}}(\boldsymbol{q}; \mathbf{c}) = -\boldsymbol{K}(\mathbf{c}) \cdot \nabla p. \tag{13}$$

In the present context, equation (13) entails a Darcy-type law, where $\boldsymbol{K}$ is a second-order permeability tensor. Note that, in line with previous works [107, 111], the convective dissipation inequality (5) is fulfilled by the convexity of $\phi^{\star}_{\text{con}}$ with respect to $\boldsymbol{q}$.

Remark 1. *In agreement with Anand [112], the present constitutive framework for porous materials can be seen as a specific case of chemomechanics. In particular, the pair $\{\zeta, p\}$ may be replaced by more general variables $\{c, \mu\}$, where c is the species concentration and μ is the chemical potential. Then, equation* (13) *plays the role of a generalized Fick's law. Furthermore, if the free energy ψ also depends on ∇c, the formulation accounts for, e.g., Cahn-Hilliard–type diffusion, as outlined in Miehe et al. [111] for elastic solids.*

At this point, starting with the Clausius-Duhem inequality (3), we have derived the constitutive relations (6). In addition, from the notion of dissipation potentials, we have obtained the evolution equations for internal variables (10) and the relation between the flux and the pressure gradient (13). These ingredients are appended to the fundamental balance laws (1) and (2) to completely determine, in strong form, the governing equations of a porous medium with gradient-extended internal variables coupled to fluid flow.

2.4. Energetic formulation of the rate-independent/rate-dependent coupled system

This section recovers the governing equations of the dissipative porous medium in a variational form, using an *extended energetic formulation* in agreement with Mielke and Roubícek [104, chapter 5]. Specifically, the rate-independent processes in the solid are coupled to the rate-dependent process of fluid transport.

2.4.1. Global energy quantities

In order to proceed with the energetic formulation, we begin by defining the required energy functionals. To this end, we first assume suitable function spaces for the primary fields and their admissible variations. The specific form of the function spaces depends on the material model; for now, we set $\mathscr{Q} \coloneqq \mathscr{U} \times \mathscr{Z} \times \mathscr{A}$, such that $\{\boldsymbol{u}, \zeta, \mathbf{a}\} \in \mathscr{Q}$. Similarly, we define the admissible test space $\tilde{\mathscr{Q}} \coloneqq \tilde{\mathscr{U}} \times \tilde{\mathscr{Z}} \times \tilde{\mathscr{A}}$, which embeds homogeneous Dirichlet boundary conditions and evolution constraints, such that $\{\tilde{\boldsymbol{u}}, \tilde{\zeta}, \tilde{\mathbf{a}}\} \in \tilde{\mathscr{Q}}$ denote admissible variations.

The internal stored energy functional reads

$$\mathcal{E}(\boldsymbol{u},\zeta,\mathbf{a}) \coloneqq \int_\Omega \psi(\boldsymbol{\varepsilon},\zeta,\mathbf{a},\nabla\mathbf{a})\,\mathrm{d}\boldsymbol{x}. \tag{14}$$

The work of mechanical loads is defined as the time integral of external power:

$$\mathcal{L}\big(\boldsymbol{u};[0,t]\big) \coloneqq \int_0^t \left[\mathcal{P}^u\big(\tau,\dot{\boldsymbol{u}}(\tau)\big) + \int_{\Gamma_{\mathrm{D}}^u} \boldsymbol{t}_{\mathrm{r}}(\tau)\cdot\dot{\boldsymbol{u}}(\tau)\,\mathrm{d}S\right]\mathrm{d}\tau, \tag{15}$$

where $\boldsymbol{t}_{\mathrm{r}}$ is the traction vector on Γ_{D}^u. The mechanical loading functional reads

$$\mathcal{P}^u(t,\dot{\boldsymbol{u}}) \coloneqq \int_\Omega \rho\boldsymbol{b}\cdot\dot{\boldsymbol{u}}\,\mathrm{d}\boldsymbol{x} + \int_{\Gamma_{\mathrm{N}}^u} \bar{\boldsymbol{t}}\cdot\dot{\boldsymbol{u}}\,\mathrm{d}S. \tag{16}$$

Rate-independent dissipative processes in the solid are characterized by the dissipation power functional

$$\mathcal{R}(\dot{\mathbf{a}};\boldsymbol{u},\zeta,\mathbf{a},\mathbf{s}) \coloneqq \int_\Omega \phi_{\mathrm{int}}(\dot{\mathbf{a}},\nabla\dot{\mathbf{a}};\mathbf{c},\mathbf{s})\,\mathrm{d}\boldsymbol{x}. \tag{17}$$

On the other hand, concerning the convective dissipation due to fluid flow, we define the viscous functional

$$\mathcal{V}(\dot{\zeta};\boldsymbol{u},\zeta,\mathbf{a}) \coloneqq \int_\Omega \bar{\phi}_{\mathrm{con}}(\dot{\zeta};\mathbf{c}) = \sup_{p\in\mathscr{P}}\left\{\int_\Omega \Big[-p\,\dot{\zeta} - \phi_{\mathrm{con}}^\star(-\nabla p;\mathbf{c})\Big]\,\mathrm{d}\boldsymbol{x} - \mathcal{P}^p(t,p)\right\}, \tag{18}$$

where $\bar{\phi}_{\mathrm{con}}$ is a 2-homogeneous function in $\dot{\zeta}$. The power of fluid injection through the boundary reads

$$\mathcal{P}^p(t,p) \coloneqq \int_{\Gamma_{\mathrm{N}}^p} p\,\bar{h}\,\mathrm{d}S. \tag{19}$$

The non-conventional expression (18) represents a *generalized Legendre transform*, extending the local transformation (12) to an integral form and accounting for boundary conditions [111]. Here, $-p$ plays the role of a dissipative stress-like variable conjugate to $\dot{\zeta}$. In the sequel, the governing equations are derived by explicitly considering the supremum in the right-hand side of equation (18). Note that the necessary conditions of this principle yield the fluid balance equations (2).

2.4.2. Evolution problem

With the energy functionals at hand, we are now able to establish an energetic formulation of the evolution problem. The first principle of the energetic formulation is energy balance, a restatement of the first law of thermodynamics given in the most general setting in a derivative-free form. The second principle is a stability condition on the rate-independent processes, given in its most general setting in a global form. In what follows, only the necessary steps to recover the governing equations are presented for the sake of brevity. Therefore, we assume sufficient regularity conditions, allowing us to state energy balance as a power balance expression. Moreover, a *local directional stability condition* is employed, from which only the first-order conditions are discussed. The reader is referred to Mielke and Roubícek [104] for a thorough account of the energetic formulation and to references [105, 113–117] for applications in solid mechanics.

In the present study, following Mielke and Roubícek [104, chapter 5], we focus on incorporating the rate-dependent fluid transport process into the originally rate-independent formulation. This is achieved by including the viscous dissipation in the statement of energy balance through the functional defined in

equation (18). We then consider that a process $\{\boldsymbol{u},\zeta,\mathbf{a}\}\colon \mathrm{T}\to\mathscr{Q}$ satisfies energy balance if the following condition holds for all $t\in\mathrm{T}$:

$$\frac{\mathrm{d}}{\mathrm{d}t}\mathcal{E}\big(\boldsymbol{u}(t),\zeta(t),\mathbf{a}(t)\big)+\mathcal{R}\big(\dot{\mathbf{a}}(t);\boldsymbol{u}(t),\zeta(t),\mathbf{a}(t),\mathbf{s}(t)\big)+2\,\mathcal{V}\big(\dot{\zeta}(t);\boldsymbol{u}(t),\zeta(t),\mathbf{a}(t)\big)-\frac{\mathrm{d}}{\mathrm{d}t}\mathcal{L}\big(\boldsymbol{u};[0,t]\big)=0. \tag{20}$$

On the other hand, a rate-independent process $\{\boldsymbol{u},\mathbf{a}\}\colon \mathrm{T}\to\mathscr{U}\times\mathscr{A}$ satisfies *first-order stability* if the following condition holds for all $t\in\mathrm{T}$:

$$\delta\mathcal{E}\big(\boldsymbol{u}(t),\zeta(t),\mathbf{a}(t)\big)\big(\tilde{\boldsymbol{u}},0,\tilde{\mathbf{a}}\big)+\mathcal{R}\big(\tilde{\mathbf{a}};\boldsymbol{u}(t),\zeta(t),\mathbf{a}(t),\mathbf{s}(t)\big)-\mathcal{P}^u(t,\tilde{\boldsymbol{u}})\geq 0\quad\forall\,\{\tilde{\boldsymbol{u}},\tilde{\mathbf{a}}\}\in\tilde{\mathscr{U}}\times\tilde{\mathscr{A}}, \tag{21}$$

with $\delta\square(\diamond)(\tilde{\diamond})$ denoting the Gâteaux derivative of a functional $\square$ in the direction $\tilde{\diamond}$. As in the case of rate-independent systems, conditions (20) and (21) provide a variational form of the governing equations of the solid phase, i.e., the mechanical balance equations (1) and the evolution equations (10). However, in the present extended framework, we also recover from (20) the evolution of the fluid phase, given in primal form as a Biot-type equation analogous to $(10)_1$ (see Miehe et al. [111] for similar derivations):

$$\frac{\partial}{\partial\zeta}\psi(\boldsymbol{\varepsilon},\zeta,\mathbf{a},\nabla\mathbf{a})+\frac{\partial}{\partial\dot{\zeta}}\bar{\phi}_{\mathrm{con}}(\dot{\zeta};\mathbf{c})=0. \tag{22}$$

Note that, in view of equation (18), the last expression entails the constitutive equation $(6)_2$.

2.5. Rate-type variational principles

The variational evolution problem (20)–(21) can be equivalently written as a rate-type stationarity principle. Formulations of this type have been widely employed in problems relevant to the present study [106, 111, 118, 119], including both *canonical minimization problems* and *saddle point problems*.

In the present formulation, the (primal) minimization problem reads

$$\inf_{\dot{\boldsymbol{u}}\in\dot{\mathscr{U}}}\inf_{\dot{\mathbf{a}}\in\dot{\mathscr{A}}}\inf_{\dot{\zeta}\in\dot{\mathscr{Z}}}\left\{\frac{\mathrm{d}}{\mathrm{d}t}\mathcal{E}(\boldsymbol{u},\zeta,\mathbf{a})+\mathcal{V}(\dot{\zeta};\boldsymbol{u},\zeta,\mathbf{a})+\mathcal{R}(\dot{\mathbf{a}};\boldsymbol{u},\zeta,\mathbf{a},\mathbf{s})-\mathcal{P}^u(t,\dot{\boldsymbol{u}})\right\}, \tag{23}$$

where the function spaces $\dot{\mathscr{U}}$, $\dot{\mathscr{Z}}$, and $\dot{\mathscr{A}}$ must account for Dirichlet boundary conditions and evolution constraints. In agreement with the energetic formulation (20)–(21), this principle yields the following necessary conditions: (i) the mechanical balance equations (1), (ii) the Biot-type evolution equations (10) for the internal variables, and (iii) the Biot-type evolution equation (22) for the fluid phase.

An apparent difficulty inherent to the canonical minimization principle (23) is that $\mathcal{V}(\dot{\zeta};\boldsymbol{u},\zeta,\mathbf{a})$ is generally not known a priori, but rather defined through the generalized Legendre transform (18) (we refer the reader to Mielke and Roubícek [104, equation 5.2.67] for a non-trivial evaluation of such a functional). Therefore, in agreement with Miehe et al. [107, 111], it is convenient to define the *mixed fluid dissipation functional*

$$\mathcal{V}^{\mathrm{M}}(\dot{\zeta},p;\boldsymbol{u},\zeta,\mathbf{a})\coloneqq\int_\Omega\Big[-p\,\dot{\zeta}-\phi^\star_{\mathrm{con}}(-\nabla p;\mathbf{c})\Big]\,\mathrm{d}\boldsymbol{x}. \tag{24}$$

This expression is replaced in (23) to yield the saddle-point problem

$$\inf_{\dot{\boldsymbol{u}}\in\dot{\mathscr{U}}}\inf_{\dot{\mathbf{a}}\in\dot{\mathscr{A}}}\inf_{\dot{\zeta}\in\dot{\mathscr{Z}}}\sup_{p\in\mathscr{P}}\left\{\frac{\mathrm{d}}{\mathrm{d}t}\mathcal{E}(\boldsymbol{u},\zeta,\mathbf{a})+\mathcal{V}^{\mathrm{M}}(\dot{\zeta},p;\boldsymbol{u},\zeta,\mathbf{a})+\mathcal{R}(\dot{\mathbf{a}};\boldsymbol{u},\zeta,\mathbf{a},\mathbf{s})-\mathcal{P}^u(t,\dot{\boldsymbol{u}})-\mathcal{P}^p(t,p)\right\}, \tag{25}$$

which is *mixed* in terms of the conjugate pair $(\dot{\zeta},-p)$ but *primal* in terms of $\boldsymbol{u}$ and $\mathbf{a}$. This principle

directly yields the following necessary conditions: (i) the mechanical balance equations (1), (ii) the Biot-type evolution equations (10) for the internal variables, (iii) the constitutive relation $(6)_2$, and (iv) the fluid balance equations (2) in terms of p.

In the following section, after presenting the ingredients of the model, the governing equations are derived by taking the saddle-point problem (25) as a point of departure. However, the local field $\dot{\zeta}$ is condensed out, resulting in an extended version of the classical $\boldsymbol{u}-p$ formulation to account for the evolution of gradient-extended internal variables. An alternative derivation is presented in appendix A, where the dependence on $\dot{\zeta}$ is a priori removed from the variational statement in a *reduced saddle-point principle*.

3. Micromechanics-based variational phase-field model coupled to fluid flow

This section presents the proposed model for fracture in fluid-saturated geomaterials. The formulation extends the model presented in Ulloa et al. [83] to hydromechanical coupling under fully saturated conditions. After a brief description of the micromechanical considerations in section 3.1, the model is constructed in section 3.2 by invoking the variational formulation presented in section 2.

3.1. Micromechanical background

As a prelude, we briefly present the local micromechanical arguments that constitute the conceptual backbone of the non-local model proposed in section 3.2. We take as a point of departure the micromechanics-based approach to damage and plasticity in quasi-brittle geomaterials [11, 12, 15] and, in particular, the extension to saturated porous media presented in Xie et al. [23]. In this context, we consider a porous material weakened by microcracks. For now, no strain localization is assumed at the macroscale and the discussion is limited to the material point level.

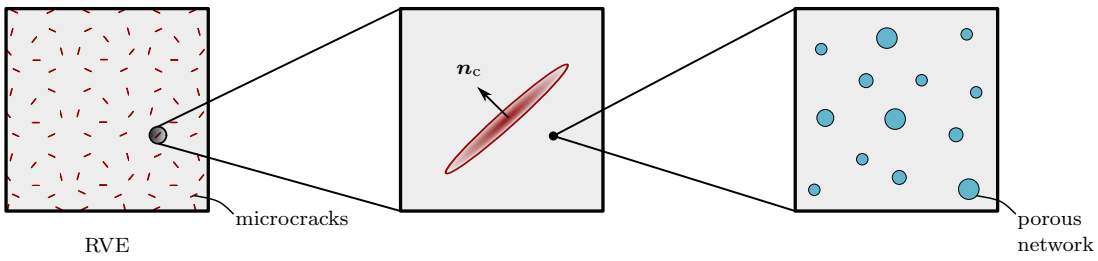

Fig. 2. Schematic representation of the RVE consisting of a matrix-inclusion system (left). The inclusions are penny-shaped microcracks with random normal orientations $\boldsymbol{n}_c$ (middle) and the matrix is a homogenized porous material (right).

As in Xie et al. [23], the main focus is the characterization of inelastic processes caused by the evolution of microcracks, namely, macroscopic damage and friction-induced plasticity. Consequently, the representative volume element (RVE) is a matrix-inclusion system with a homogenized porous matrix material and a set of randomly distributed penny-shaped microcracks, assumed to be much smaller than the RVE (figure 2). The

matrix material is linear (poro-) elastic and isotropic, characterized by the fourth-order elasticity tensor[2]

$$\mathbf{C} = K\mathbf{1}\otimes\mathbf{1} + 2\mu\left(\mathsf{I} - \frac{1}{3}\mathbf{1}\otimes\mathbf{1}\right), \tag{26}$$

where $\mathbf{1}$ and I denote the second- and fourth-order identity tensors. The bulk and shear moduli K and μ describe the elastic behavior of the porous matrix material and are thus presumably smaller than the corresponding stiffness parameters of the solid phase K^{s} and μ^{s}. The intrinsic energy dissipation of the RVE is induced by the microcracks embedded in the porous matrix. For simplicity, a uniform distribution of microcracks in all directions is assumed, consistent with a direction-independent characterization of damage and an isotropic effective behavior of the RVE [1]. In this context, we shall be concerned with two possible macroscopic scenarios: (i) a state of opening microcracks in a *tensile regime* and (ii) a state of closed microcracks subject to frictional sliding in a *compressive/shear* regime.

In the case of opening microcracks, the macroscopic elasticity tensor of the RVE takes the form

$$\mathbf{C}^{\mathrm{hom}}(\omega) = K^{\mathrm{hom}}(\omega)\mathbf{1}\otimes\mathbf{1} + 2\mu^{\mathrm{hom}}(\omega)\left(\mathsf{I} - \frac{1}{3}\mathbf{1}\otimes\mathbf{1}\right), \tag{27}$$

where ω is an internal variable directly related to the microcrack density [15]. The macroscopic bulk and shear moduli $K^{\mathrm{hom}}(\omega)$ and $\mu^{\mathrm{hom}}(\omega)$ follow from a suitable homogenization scheme. For instance, considering the Mori-Tanaka scheme [121], one has[3]

$$K^{\mathrm{hom}}(\omega) = \frac{K}{1+b_K\omega} \quad\text{and}\quad \mu^{\mathrm{hom}}(\omega) = \frac{\mu}{1+b_\mu\omega} \quad\text{with}\quad b_K = \frac{16}{9}\frac{1-\nu^2}{1-2\nu}\,, \quad b_\mu = \frac{32}{45}\frac{(1-\nu)(5-\nu)}{2-\nu}\,, \tag{28}$$

where ν is the Poisson's ratio of the porous matrix material. Then, the macroscopic free energy density of the RVE can be written in agreement with Coussy [26] as

$$\psi^{\mathrm{open}}(\boldsymbol{\varepsilon},\zeta,\omega) = \frac{1}{2}\,\boldsymbol{\varepsilon} : \mathbf{C}^{\mathrm{hom}}(\omega) : \boldsymbol{\varepsilon} + \frac{M^{\mathrm{hom}}(\omega)}{2}\big(B^{\mathrm{hom}}(\omega)\,\mathrm{tr}\,\boldsymbol{\varepsilon} - \zeta\big)^2. \tag{29}$$

Note that equation $(6)_2$ yields $p^{\mathrm{open}} = -M\big(B^{\mathrm{hom}}(\omega)\,\mathrm{tr}\,\boldsymbol{\varepsilon} - \zeta\big)$. Thus, for $p^{\mathrm{open}} = 0$, the second term in (29) vanishes, recovering the macroscopic free energy density of a dry material. On the other hand, in a saturated material, $\omega \mapsto B^{\mathrm{hom}}(\omega)$ gives the macroscopic Biot coefficient and $\omega \mapsto M^{\mathrm{hom}}(\omega)$ gives the macroscopic Biot modulus, both accounting for the effect of fluid-filled open microcracks. In particular, one has [1, 22, 23]

$$B^{\mathrm{hom}}(\omega) = 1 - \frac{K^{\mathrm{hom}}(\omega)}{K^{\mathrm{s}}} = B + (1-B)\left(1 - \frac{K^{\mathrm{hom}}(\omega)}{K}\right) = B + (1-B)\frac{b_K\omega}{1+b_K\omega}\,, \tag{30}$$

$$\frac{1}{M^{\mathrm{hom}}(\omega)} = \frac{1}{K^{\mathrm{s}}}\big(B^{\mathrm{hom}}(\omega) - \vartheta_0^{\mathrm{f}}\big) = \frac{1}{M} + \frac{1}{K^{\mathrm{s}}}(1-B)\left(1 - \frac{K^{\mathrm{hom}}(\omega)}{K}\right) = \frac{1}{M} + \frac{1}{K^{\mathrm{s}}}(1-B)\frac{b_K\omega}{1+b_K\omega}\,. \tag{31}$$

On the right-hand side of these expressions, $B = 1 - K/K^{\mathrm{s}}$ and $1/M = (B - \vartheta_0^{\mathrm{f}})/K^{\mathrm{s}}$ denote the Biot

[2]We note that the present scheme implies a separation of scales between the microcrack network and the saturated porous microstructure, the latter being defined at a smaller scale. A similar treatment can be found in recent computational homogenization schemes for porous rocks [120]. Of course, a full micromechanical analysis of the present model would imply a micromechanical treatment of the porous matrix as well. However, this topic is out of scope in the present study.

[3]In this work, the Mori-Tanaka scheme is chosen as a specific example, in agreement with the cited references on the micromechanics-based modeling of dry and saturated rock-like materials with microcracks [1, 23, 24]. Of course, different choices, e.g., the Ponte-Castaneda and Willis scheme, can be equally made at this point.

parameters of the undamaged porous matrix, while the second terms represent the contribution of open microcracks. Note that the constant parameters are recovered as the microcrack density vanishes ($\omega \to 0$).

On the other hand, in the compressive/shear regime, the free energy must account for the frictional sliding of closed microcracks. This mechanism calls for the introduction of a plastic strain tensor $\boldsymbol{\varepsilon}^{\mathrm{p}}$, directly linked to the averaged displacement discontinuities across the surfaces of frictional microcracks in the RVE [12, 15]. Moreover, in view of the small strain hypothesis, the macroscopic strain tensor $\boldsymbol{\varepsilon}$ is decomposed as

$$\boldsymbol{\varepsilon} = \boldsymbol{\varepsilon}^{\mathrm{e}} + \boldsymbol{\varepsilon}^{\mathrm{p}}, \tag{32}$$

where $\boldsymbol{\varepsilon}^{\mathrm{e}}$ denotes the elastic strain tensor. The corresponding macroscopic free energy density accounting for the porous nature of the matrix is derived in Xie et al. [23]. Here, we state this quantity as

$$\psi^{\mathrm{close}}(\boldsymbol{\varepsilon}, \zeta, \boldsymbol{\varepsilon}^{\mathrm{p}}, \omega) = \frac{1}{2}(\boldsymbol{\varepsilon} - \boldsymbol{\varepsilon}^{\mathrm{p}}) : \mathbf{C} : (\boldsymbol{\varepsilon} - \boldsymbol{\varepsilon}^{\mathrm{p}}) + \frac{1}{2}\,\boldsymbol{\varepsilon}^{\mathrm{p}} : \mathbf{H}^{\mathrm{block}}(\omega) : \boldsymbol{\varepsilon}^{\mathrm{p}} + \frac{M}{2}\big[B\,\mathrm{tr}(\boldsymbol{\varepsilon} - \boldsymbol{\varepsilon}^{\mathrm{p}}) - (\zeta - \mathrm{tr}\,\boldsymbol{\varepsilon}^{\mathrm{p}})\big]^2. \tag{33}$$

Note that equation $(6)_2$ yields $p^{\mathrm{close}} = -M\big[B\,\mathrm{tr}(\boldsymbol{\varepsilon} - \boldsymbol{\varepsilon}^{\mathrm{p}}) - (\zeta - \mathrm{tr}\,\boldsymbol{\varepsilon}^{\mathrm{p}})\big]$. Thus, for $p^{\mathrm{close}} = 0$, equation (33) recovers the macroscopic energy derived for the case of dry materials in Zhu et al. [15]. The first term in (33) then represents the elastic strain energy stored in the solid matrix, while the second term represents the energy *blocked* on the surface of frictional microcracks. These terms constitute a quadratic elastoplastic energy density with kinematic hardening, revealing the frictional sliding of microcracks as the microscopic origin of plasticity in quasi-brittle materials. However, in contrast with purely phenomenological hardening/softening models, the function $\omega \mapsto \mathbf{H}^{\mathrm{block}}(\omega)$ directly follows from the coupling between microcrack growth and frictional sliding and does not require phenomenological assumptions. Instead, it is derived from imposing, at the transition between the open/closed states, continuous differentiability of the free energy, i.e., equivalence between expressions (29) and (33) as well as their first derivatives. These conditions yield [15, 83]

$$\mathbf{H}^{\mathrm{block}}(\omega) = \Big[\mathbf{C}^{\mathrm{hom}\,-1}(\omega) - \mathbf{C}^{-1}\Big]^{-1} = \frac{K}{b_K\omega}\mathbf{1}\otimes\mathbf{1} + \frac{2\mu}{b_\mu\omega}\left(\mathbf{I} - \frac{1}{3}\mathbf{1}\otimes\mathbf{1}\right). \tag{34}$$

In a saturated material, the last term in (33) further accounts for the pressurizing fluid. Note that its form is in agreement with, e.g., Coussy [26]. In this term, $\zeta - \mathrm{tr}\,\boldsymbol{\varepsilon}^{\mathrm{p}}$ represents a reversible variation of fluid content, with $\mathrm{tr}\,\boldsymbol{\varepsilon}^{\mathrm{p}}$ representing a *plastic variation of fluid content*. In the present framework, this mechanism is solely due to the volumetric plastic deformations induced by the sliding of frictional microcracks. Therefore, no plastic changes occur in the porous matrix material (figure 2).

Remark 2. *The cited references on the adopted micromechanical theory [22, 23] present the formulation in terms of the* grand-canonical energy density $\psi^{\mathrm{f}\star} = \psi - p\,\zeta$*, replacing the dependence on* ζ *by dependence on* p*. This equivalent approach is employed in the reduced saddle-point principle presented in appendix A.*

At this point, according to the formulation presented in section 2, a thermodynamically admissible dissipation potential may be defined to establish the governing equations of the model. However, the formulation above is inherently local and therefore unsuitable for damaging solids with strain localization at the macroscale. Thus, as in Ulloa et al. [83], we first replace the local internal variable ω with a gradient-extended variable, i.e., with the *crack phase-field*. The proposed model is described in the remainder of this section.

3.2. The proposed micromechanics-based phase-field model

A phase-field model is now constructed by taking the micromechanical arguments of the previous section as a point of departure and rigorously following the variational formulation presented in section 2. As such, the free energy density is first defined, followed by the intrinsic and convective dissipation potentials, which consider microcrack growth, frictional sliding, and fluid transport. The free energy and the dissipation potentials are then taken as inputs to derive the governing equations from the variational principle (25).

3.2.1. Free energy density and constitutive relations

As in section 2, consider the response of a porous solid in $\Omega \times \mathrm{T}$ with possible localization and fracture. Adopting the phase-field approach to fracture, the response of the solid is characterized by the displacement field $\boldsymbol{u}\colon \Omega\times\mathrm{T} \to \mathbb{R}^3$ and the crack phase-field $\alpha\colon \Omega\times\mathrm{T} \to [0,1]$, where intact material points and completely fractured material points are given by $\alpha(\boldsymbol{x},t) = 0$ and $\alpha(\boldsymbol{x},t) = 1$, respectively. The plastic strain tensor $\boldsymbol{\varepsilon}^{\mathrm{p}}\colon \Omega\times\mathrm{T} \to \mathbb{R}^{3\times3}_{\mathrm{sym}}$ represents a macroscopic measure of the frictional sliding of closed microcracks, while the pore pressure field $p\colon \Omega\times\mathrm{T} \to \mathbb{R}$ characterizes the fluid flow. The different mechanisms and their interactions in the multiphysics model are depicted in figure 3 and discussed in detail in the following paragraphs.

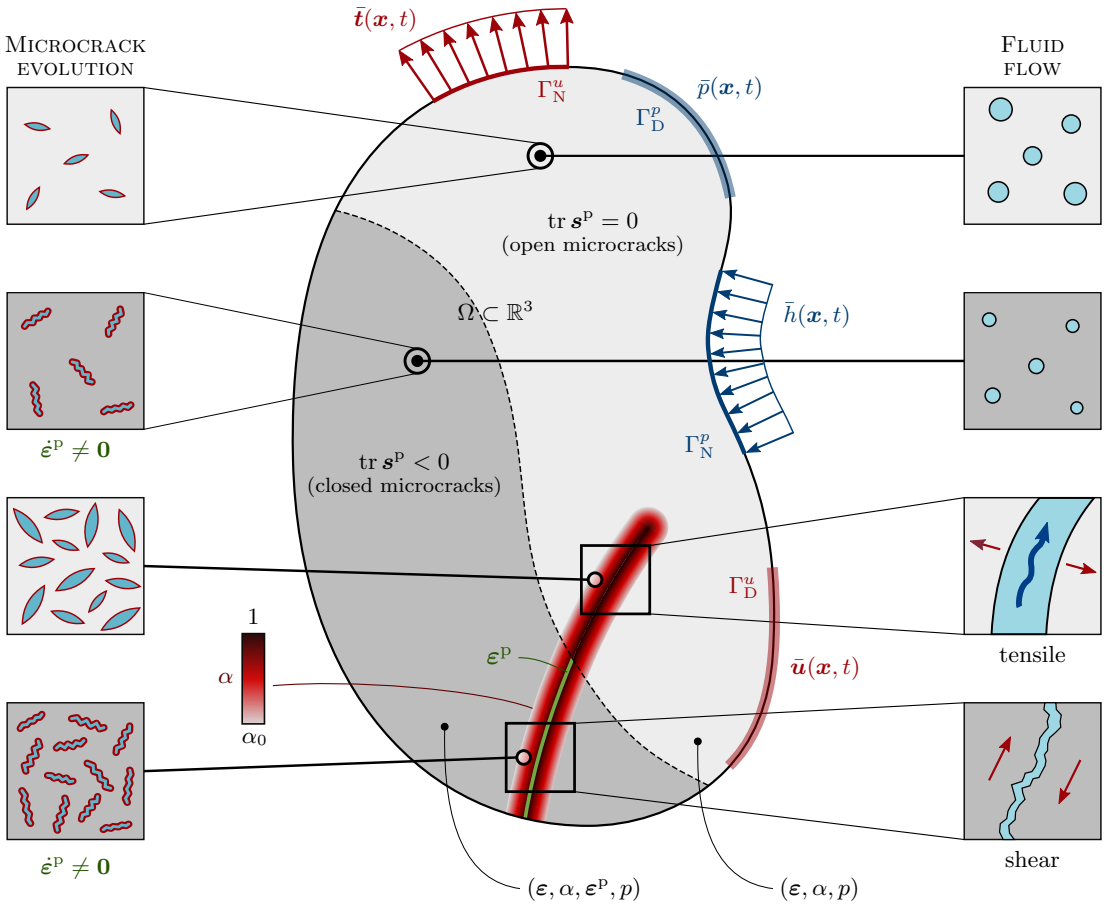

Fig. 3. Schematic representation of the multiphysics boundary value problem and the mechanisms of the proposed model, showing the microcrack evolution and the fluid flow in both the compressive/shear and the tensile regimes.

Let us begin the formulation by defining the macroscopic elasticity tensor and the consequences thereof.

The fundamental idea is to restate the ω-dependent tensor (27) as a function of the crack phase-field via

$$\mathbf{C}^{\mathrm{hom}}(\omega) \equiv \mathbf{C}^{\mathrm{dam}}(\alpha), \tag{35}$$

which provides a direct relation between the microcrack density parameter and the crack phase-field, i.e., $\omega = \omega(\alpha)$, depending on the degradation functions $g_K(\alpha)$ and $g_\mu(\alpha)$ and the micromechanics-based quantities $K^{\mathrm{hom}}(\omega)$ and $\mu^{\mathrm{hom}}(\omega)$. In view of isotropic behavior, the function $\alpha \mapsto \mathbf{C}^{\mathrm{dam}}(\alpha)$ reads

$$\mathbf{C}^{\mathrm{dam}}(\alpha) \coloneqq g_K(\alpha) K \mathbf{1} \otimes \mathbf{1} + 2\, g_\mu(\alpha) \mu \left(\mathbf{I} - \frac{1}{3} \mathbf{1} \otimes \mathbf{1} \right). \tag{36}$$

Considering the Mori-Tanaka scheme, equations (27), (28), and (36) imply that

$$\omega(\alpha) = \frac{1 - g_K(\alpha)}{b_K\, g_K(\alpha)} \qquad \text{and} \qquad \omega(\alpha) = \frac{1 - g_\mu(\alpha)}{b_\mu\, g_\mu(\alpha)}\,. \tag{37}$$

Thus, the functions $g_K(\alpha)$ and $g_\mu(\alpha)$ may not be defined independently. In the present study, we set

$$g_K(\alpha) \coloneqq \frac{(1-\alpha)^2}{1 + (b-1)[1 - (1-\alpha)^2]}\,. \tag{38}$$

This function, taken from Alessi et al. [122] and also employed in the previous related works on dry materials [83, 84], includes a single tuning parameter b. This parameter allows us to recover the more common quadratic version $(1-\alpha)^2$ for $b = 1$ and to consider a smoother softening stage, i.e., a less brittle response, for $b > 1$. Using equation (37), we derive the shear degradation function

$$g_\mu(\alpha) = \frac{g_K(\alpha)}{g_K(\alpha) + \frac{b_\mu}{b_K}[1 - g_K(\alpha)]}\,. \tag{39}$$

Note from equations (37), (38), and (39) that a complete damage process $\alpha \to 1$ and vanishing damage $\alpha \to 0$ correspond to $\omega \to \infty$ and $\omega \to 0$, respectively.

Using the ansatz (35), the constitutive functions (30), (31), and (34) are restated as functions of α via

$$B^{\mathrm{hom}}(\omega(\alpha)) \equiv B^{\mathrm{dam}}(\alpha) = 1 - \frac{K^{\mathrm{dam}}(\alpha)}{K^{\mathrm{s}}} = B + (1-B)\big(1 - g_K(\alpha)\big), \tag{40}$$

$$\frac{1}{M^{\mathrm{hom}}(\omega(\alpha))} \equiv \frac{1}{M^{\mathrm{dam}}(\alpha)} = \frac{1}{K^{\mathrm{s}}}\big(B^{\mathrm{dam}}(\alpha) - \vartheta_0^{\mathrm{f}}\big) = \frac{1}{M} + \frac{1}{K}(1-B)^2\big(1 - g_K(\alpha)\big), \tag{41}$$

$$\mathbf{H}^{\mathrm{block}}(\omega(\alpha)) \equiv \mathbf{H}^{\mathrm{kin}}(\alpha) = \Big[\mathbf{C}^{\mathrm{dam}\,-1}(\alpha) - \mathbf{C}^{-1} \Big]^{-1} = H_K^{\mathrm{kin}}(\alpha) \mathbf{1} \otimes \mathbf{1} + H_\mu^{\mathrm{kin}}(\alpha) \left(\mathbf{I} - \frac{1}{3} \mathbf{1} \otimes \mathbf{1} \right), \tag{42}$$

where the damage-dependent kinematic hardening moduli read

$$H_K^{\mathrm{kin}}(\alpha) = \frac{g_K(\alpha) K}{1 - g_K(\alpha)} \qquad \text{and} \qquad H_\mu^{\mathrm{kin}}(\alpha) = \frac{2\, g_\mu(\alpha) \mu}{1 - g_\mu(\alpha)}\,. \tag{43}$$

Note that the constitutive functions above follow directly from the degradation functions $g_K(\alpha)$ and $g_\mu(\alpha)$.

In view of the homogenized energy densities (29) and (33) for porous solids with *open* and *closed* micro-

cracks, and labeling these cases as open and closed hereinafter, the free energy density reads

$$\psi(\boldsymbol{\varepsilon},\zeta,\boldsymbol{\varepsilon}^{\mathrm{p}},\alpha)=\begin{cases}\dfrac{1}{2}\,\boldsymbol{\varepsilon}:\mathbf{C}^{\mathrm{dam}}(\alpha):\boldsymbol{\varepsilon}+\dfrac{M^{\mathrm{dam}}(\alpha)}{2}\big(B^{\mathrm{dam}}(\alpha)\,\mathrm{tr}\,\boldsymbol{\varepsilon}-\zeta\big)^2 & \text{if open,}\\[2ex] \dfrac{1}{2}(\boldsymbol{\varepsilon}-\boldsymbol{\varepsilon}^{\mathrm{p}}):\mathbf{C}:(\boldsymbol{\varepsilon}-\boldsymbol{\varepsilon}^{\mathrm{p}})+\dfrac{1}{2}\,\boldsymbol{\varepsilon}^{\mathrm{p}}:\mathbf{H}^{\mathrm{kin}}(\alpha):\boldsymbol{\varepsilon}^{\mathrm{p}}+\dfrac{M}{2}\big[B\,\mathrm{tr}(\boldsymbol{\varepsilon}-\boldsymbol{\varepsilon}^{\mathrm{p}})-(\zeta-\mathrm{tr}\,\boldsymbol{\varepsilon}^{\mathrm{p}})\big]^2 & \text{if closed.}\end{cases} \tag{44}$$

The constitutive equations (6) yield the stress-strain relation

$$\boldsymbol{\sigma}(\boldsymbol{\varepsilon},\zeta,\boldsymbol{\varepsilon}^{\mathrm{p}},\alpha)=\frac{\partial\psi}{\partial\boldsymbol{\varepsilon}}=\begin{cases}\mathbf{C}^{\mathrm{dam}}(\alpha):\boldsymbol{\varepsilon}+B^{\mathrm{dam}}(\alpha)\,M^{\mathrm{dam}}(\alpha)(B^{\mathrm{dam}}(\alpha)\,\mathrm{tr}\,\boldsymbol{\varepsilon}-\zeta)\mathbf{1} & \text{if open,}\\ \mathbf{C}:(\boldsymbol{\varepsilon}-\boldsymbol{\varepsilon}^{\mathrm{p}})+BM\big[B\,\mathrm{tr}(\boldsymbol{\varepsilon}-\boldsymbol{\varepsilon}^{\mathrm{p}})-(\zeta-\mathrm{tr}\,\boldsymbol{\varepsilon}^{\mathrm{p}})\big]\mathbf{1} & \text{if closed,}\end{cases} \tag{45}$$

and the constitutive relation between the pressure and the fluid content variation

$$p(\boldsymbol{\varepsilon},\zeta,\boldsymbol{\varepsilon}^{\mathrm{p}},\alpha)=\frac{\partial\psi}{\partial\zeta}=\begin{cases}-M^{\mathrm{dam}}(\alpha)(B^{\mathrm{dam}}(\alpha)\,\mathrm{tr}\,\boldsymbol{\varepsilon}-\zeta) & \text{if open,}\\ -M\big[B\,\mathrm{tr}(\boldsymbol{\varepsilon}-\boldsymbol{\varepsilon}^{\mathrm{p}})-(\zeta-\mathrm{tr}\,\boldsymbol{\varepsilon}^{\mathrm{p}})\big] & \text{if closed.}\end{cases} \tag{46}$$

Similarly, we obtain the generalized stress conjugate to the plastic strain tensor

$$\boldsymbol{s}^{\mathrm{p}}(\boldsymbol{\varepsilon},\zeta,\boldsymbol{\varepsilon}^{\mathrm{p}},\alpha)=-\frac{\partial\psi}{\partial\boldsymbol{\varepsilon}^{\mathrm{p}}}=\begin{cases}\mathbf{0} & \text{if open,}\\ \mathbf{C}:(\boldsymbol{\varepsilon}-\boldsymbol{\varepsilon}^{\mathrm{p}})-\mathbf{H}^{\mathrm{kin}}(\alpha):\boldsymbol{\varepsilon}^{\mathrm{p}}-M\big[B\,\mathrm{tr}(\boldsymbol{\varepsilon}-\boldsymbol{\varepsilon}^{\mathrm{p}})-(\zeta-\mathrm{tr}\,\boldsymbol{\varepsilon}^{\mathrm{p}})\big](1-B)\mathbf{1} & \text{if closed.}\end{cases} \tag{47}$$

Note that equation (47) naturally embeds the microcrack opening/closure condition through $\boldsymbol{s}^{\mathrm{p}}=\mathbf{0}$. Thus, in view of isotropic behavior, we employ the conditions

$$\begin{cases}\mathrm{tr}\,\boldsymbol{s}^{\mathrm{p}}(\boldsymbol{\varepsilon},\zeta,\boldsymbol{\varepsilon}^{\mathrm{p}},\alpha)=0 & \text{if open,}\\ \mathrm{tr}\,\boldsymbol{s}^{\mathrm{p}}(\boldsymbol{\varepsilon},\zeta,\boldsymbol{\varepsilon}^{\mathrm{p}},\alpha)<0 & \text{if closed}\end{cases} \tag{48}$$

to signal open microcrack states in the tensile regime and closed microcrack states in the compressive/shear regime (figure 3). Finally, the generalized stress conjugate to the crack phase-field reads

$$s^{\mathrm{d}}(\boldsymbol{\varepsilon},\zeta,\boldsymbol{\varepsilon}^{\mathrm{p}},\alpha)=-\frac{\partial\psi}{\partial\alpha}=\begin{cases}-\dfrac{1}{2}\,\boldsymbol{\varepsilon}:\mathbf{C}^{\mathrm{dam}\prime}(\alpha):\boldsymbol{\varepsilon}+\dfrac{\partial}{\partial\alpha}\left(\dfrac{M^{\mathrm{dam}}(\alpha)}{2}\big(B^{\mathrm{dam}}(\alpha)\,\mathrm{tr}\,\boldsymbol{\varepsilon}-\zeta\big)^2\right) & \text{if open,}\\[2ex] -\dfrac{1}{2}\,\boldsymbol{\varepsilon}^{\mathrm{p}}:\mathbf{H}^{\mathrm{kin}\prime}(\alpha):\boldsymbol{\varepsilon}^{\mathrm{p}} & \text{if closed.}\end{cases} \tag{49}$$

According to this expression, damage in the open state is driven by poroelastic energy, while damage in the closed state is solely driven by the blocked plastic energy that results from frictional sliding.

For subsequent developments, we further note that in view of equation (46), equations (45), (47), and (49) equivalently read (with an abuse of notation)

$$\boldsymbol{\sigma}(\boldsymbol{\varepsilon},p,\boldsymbol{\varepsilon}^{\mathrm{p}},\alpha)=\begin{cases}\mathbf{C}^{\mathrm{dam}}(\alpha):\boldsymbol{\varepsilon}-B^{\mathrm{dam}}(\alpha)\,p\mathbf{1} & \text{if open,}\\ \mathbf{C}:(\boldsymbol{\varepsilon}-\boldsymbol{\varepsilon}^{\mathrm{p}})-B\,p\mathbf{1} & \text{if closed,}\end{cases} \tag{50}$$

revealing that $\boldsymbol{\sigma}$ is in agreement with Biot's effective stress;

$$\boldsymbol{s}^{\mathrm{p}}(\boldsymbol{\varepsilon}, p, \boldsymbol{\varepsilon}^{\mathrm{p}}, \alpha) = \begin{cases} \mathbf{0} & \text{if open,} \\ \mathbf{C} : (\boldsymbol{\varepsilon} - \boldsymbol{\varepsilon}^{\mathrm{p}}) - \mathbf{H}^{\mathrm{kin}}(\alpha) : \boldsymbol{\varepsilon}^{\mathrm{p}} - B\, p\mathbf{1} + p\mathbf{1} & \text{if closed,} \end{cases} \tag{51}$$

revealing that the *plastic driving force* takes the form of Terzaghi's effective stress (cf. Zhao and Borja [123]) in terms of $\boldsymbol{s}^{\mathrm{p}}$ in the compressive/shear regime; and

$$s^{\mathrm{d}}(\boldsymbol{\varepsilon}, p, \boldsymbol{\varepsilon}^{\mathrm{p}}, \alpha) = \begin{cases} -\dfrac{1}{2K}\, g_K'(\alpha)\, (K \operatorname{tr}\boldsymbol{\varepsilon} - Bp + p)^2 - g_\mu'(\alpha)\, \mu\, \boldsymbol{\varepsilon}_{\mathrm{dev}} : \boldsymbol{\varepsilon}_{\mathrm{dev}} & \text{if open,} \\ -\dfrac{1}{2}\, H_K^{\mathrm{kin}\prime}(\alpha)(\operatorname{tr}\boldsymbol{\varepsilon}^{\mathrm{p}})^2 - \dfrac{1}{2}\, H_\mu^{\mathrm{kin}\prime}(\alpha)\, \boldsymbol{\varepsilon}^{\mathrm{p}}_{\mathrm{dev}} : \boldsymbol{\varepsilon}^{\mathrm{p}}_{\mathrm{dev}} & \text{if closed,} \end{cases} \tag{52}$$

where we have also used equations (40)–(42), revealing that damage in the open state is driven by elastic energy in terms of Terzaghi's effective stress (cf. [1, equation 10.102] for $B = 0$). From these expressions, one observes that setting $B = 0$ in the open state uncouples the fluid pressure from the total stress but not from the damage driving force. Thus, if the influence of fluid pressure in the porous matrix is neglected, the fluid pressure remains active in the opening microcracks and drives damage. Conversely, in the closed state, the damage driving force does not depend on the fluid pressure. Indeed, because the matrix is poroelastic, the plastic-damage response is solely due to microcrack growth and frictional sliding. Moreover, setting $B = 0$ in the closed state uncouples the fluid pressure from the total stress but not from the plastic driving force. In this case, if the influence of fluid pressure in the porous matrix is neglected, the fluid pressure modulates the volumetric plastic component of sliding microcracks but does not promote damage directly.

It is worth recalling that the piecewise conjugate variables (45), (46), (47), and (49) are continuous due to the continuous differentiability of the free energy, as ensured by the structure of the kinematic hardening tensor (42). As discussed in Ulloa et al. [83] for the case of dry materials, owing to the micromechanical considerations, the present model presents some interesting features that are not present in conventional phase-field models. In particular, by virtue of equation (44), the present model embeds a natural distinction between a tensile-brittle regime and a compressive-ductile regime, associated with opening microcracks and frictional sliding, respectively. This feature allows us to capture different failure modes and to preclude unrealistic compressive fracture without introducing heuristic energy splits. Moreover, when compared to phase-field models for ductile fracture, by virtue of equation (43), the present model does not require the definition of phenomenological hardening parameters or plastic degradation functions. Note further that for $\alpha \to 0$, the functions in (43) approach infinity, yielding an elastic response and implying that no frictional sliding can occur in the absence of microcracks. In the present work, these features are further enhanced by taking into account the effect of pore pressure, as described in the preceding passages.

3.2.2. Dissipation potentials

As discussed in section 2.3, the adopted variational framework requires the definition of the intrinsic dissipation potential ϕ_{int} and the convective dissipation ϕ_{con}, the latter being alternatively defined in terms of its convex conjugate $\phi^\star_{\mathrm{con}}$ through equation (12). Let us address these constitutive functions below.

Intrinsic dissipation. The intrinsic dissipation potential characterizes the evolution of the internal variables $\boldsymbol{\varepsilon}^{\mathrm{p}}$ and α, and it is additively decomposed into a plastic contribution ϕ^{p} and a fracture contribution ϕ^{d}:

$$\phi_{\mathrm{int}}(\dot{\boldsymbol{\varepsilon}}^{\mathrm{p}}, \dot{\alpha}, \nabla\dot{\alpha}; \alpha, \nabla\alpha, \boldsymbol{s}^{\mathrm{p}}) = \phi^{\mathrm{p}}(\dot{\boldsymbol{\varepsilon}}^{\mathrm{p}}; \boldsymbol{s}^{\mathrm{p}}) + \phi^{\mathrm{d}}(\dot{\alpha}, \nabla\dot{\alpha}; \alpha, \nabla\alpha, \boldsymbol{s}^{\mathrm{p}}). \tag{53}$$

Despite the dependence of $\boldsymbol{s}^{\mathrm{p}}$ on the pore pressure, these functions take the same forms presented in Ulloa et al. [105] for dry materials; the main arguments are summarized below for the reader's convenience.

$$\dot{\boldsymbol{\varepsilon}}^{\mathrm{p}} \in \begin{cases} \lambda \left(\sqrt{\frac{2}{3}} A_{\varphi} \mathbf{1} + \partial \| \tilde{\boldsymbol{s}}^{\mathrm{p}}_{\mathrm{dev}} \| \right) & \text{Associative flow} \\ \lambda \left(\sqrt{\frac{2}{3}} A_{\theta} \mathbf{1} + \partial \| \tilde{\boldsymbol{s}}^{\mathrm{p}}_{\mathrm{dev}} \| \right) & \text{Non-associative flow} \end{cases}$$

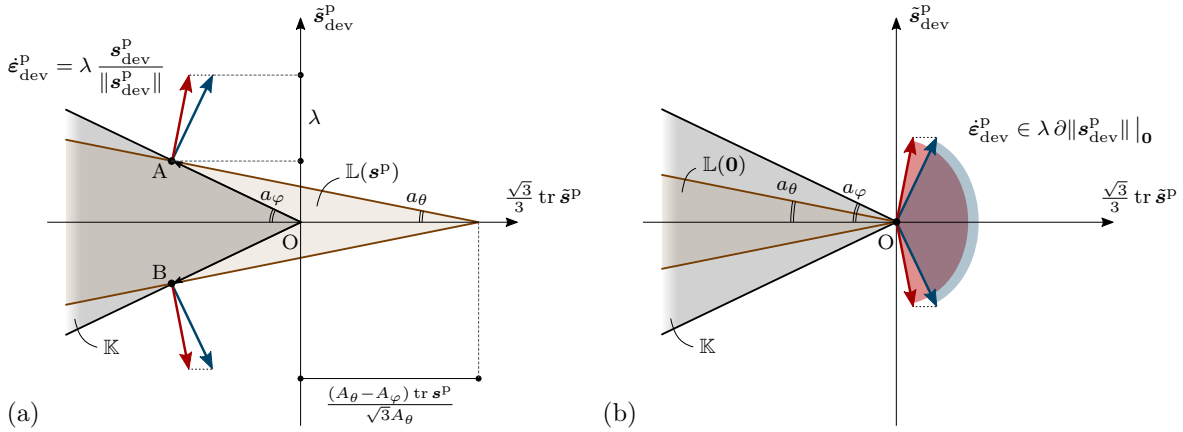

Fig. 4. Elastic domain $\mathbb{K}$ (gray region) and state-dependent domain $\mathbb{L}(\boldsymbol{s}^{\mathrm{p}})$ (brown region) for the Drucker-Prager model: (a) flow rule at states $\pm\boldsymbol{s}^{\mathrm{p}}$ (A and B), corresponding to smooth points of $\mathbb{K}$ and $\mathbb{L}(\boldsymbol{s}^{\mathrm{p}})$, and (b) flow rule at the apex. The tensors normal to $\partial\mathbb{L}(\boldsymbol{s}^{\mathrm{p}})$ (red) correspond to the non-associative flow rule, while the tensors normal to $\partial\mathbb{K}$ (blue) recover the associative case where the volumetric plastic strain rate is larger. Here, $\tan a_{\varphi} = \sqrt{2}A_{\varphi}$ and $\tan a_{\theta} = \sqrt{2}A_{\theta}$.

The plastic contribution follows from the definition of the plasticity evolution equations in generalized stress space. Thus, in order to consider non-associative flow, we first define the *plastic yield function* f^{p} and the *plastic potential* g^{p}:

$$f^{\mathrm{p}}(\boldsymbol{s}^{\mathrm{p}}) := \|\boldsymbol{s}^{\mathrm{p}}_{\mathrm{dev}}\| + \sqrt{\frac{2}{3}} A_{\varphi} \mathrm{tr}\boldsymbol{s}^{\mathrm{p}} \qquad \text{and} \qquad g^{\mathrm{p}}(\boldsymbol{s}^{\mathrm{p}}) := \|\boldsymbol{s}^{\mathrm{p}}_{\mathrm{dev}}\| + \sqrt{\frac{2}{3}} A_{\theta} \mathrm{tr}\boldsymbol{s}^{\mathrm{p}}. \tag{54}$$

The condition $f^{\mathrm{p}}(\boldsymbol{s}^{\mathrm{p}}) \leq 0$ can be viewed as a friction criterion on the (isotropic) local stress field $\boldsymbol{s}^{\mathrm{p}}$, taking the form of a Drucker-Prager model at the macroscale. Here, A_{φ} is the friction coefficient and A_{θ} is the dilation coefficient, with $0 \leq A_{\theta} \leq A_{\varphi}$. Note that $f^{\mathrm{p}}(\boldsymbol{s}^{\mathrm{p}})$ does not include a cohesive term in generalized stress space in order for $\boldsymbol{s}^{\mathrm{p}}_{\mathrm{dev}}$ to vanish at the opening/closure transition (equation (48)). However, by virtue of both the back-tress term $\mathbf{H}^{\mathrm{kin}}(\alpha) : \boldsymbol{\varepsilon}^{\mathrm{p}}$ and the pore pressure term $p\mathbf{1}$ (for $B < 1$) in equation (51), a damage- and pressure-dependent cohesion is attained in terms of the effective stress $\mathbf{C} : (\boldsymbol{\varepsilon} - \boldsymbol{\varepsilon}^{\mathrm{p}})$. With these definitions, the classical plasticity evolution equations consist of the generalized stress constraint

$$\boldsymbol{s}^{\mathrm{p}} \in \mathbb{K} := \left\{ \boldsymbol{s}^{\mathrm{p}} \in \mathbb{R}^{3\times 3}_{\mathrm{sym}} \;\middle|\; f^{\mathrm{p}}(\boldsymbol{s}^{\mathrm{p}}) \leq 0 \right\}, \tag{55}$$

where the convex set $\mathbb{K}$ represents the elastic domain, and the non-associative flow rule (see figure 4)

$$\dot{\boldsymbol{\varepsilon}}^{\mathrm{p}} \in \mathbb{Q}(\boldsymbol{s}^{\mathrm{p}}) := \left\{ \lambda\, \hat{\boldsymbol{n}} \in \mathbb{R}^{3\times 3}_{\mathrm{sym}} \;\middle|\; \hat{\boldsymbol{n}} \in \partial g^{\mathrm{p}}(\boldsymbol{s}^{\mathrm{p}});\ \lambda \geq 0,\ \lambda = 0 \text{ if } f^{\mathrm{p}}(\boldsymbol{s}^{\mathrm{p}}) < 0 \right\}. \tag{56}$$

Clearly, if $A_{\theta} = A_{\varphi}$, we recover the associative model. In that case, the volumetric plastic strains are modulated by the friction coefficient A_{φ}. However, the non-associative model is preferred due to (i) its more

realistic description of geomaterial behavior and failure [3, 124] and (ii) the fact that the associative model leads to an unphysical vanishing plastic dissipation.

The main implication of adopting a non-associative flow rule is that the variational structure inherent to associative models is seemingly lost. In order to address this apparent deficiency and allow for a variational formulation of the present model, we follow the framework presented in Ulloa et al. [105] and introduce a state-dependent set of generalized stresses (figure 4)

$$\mathbb{L}(\boldsymbol{s}^{\mathrm{p}}) \coloneqq \left\{ \tilde{\boldsymbol{s}}^{\mathrm{p}} \in \mathbb{R}^{3\times 3}_{\mathrm{sym}} \;\; | \;\; \|\tilde{\boldsymbol{s}}^{\mathrm{p}}_{\mathrm{dev}}\| + \sqrt{\frac{2}{3}} A_\theta \operatorname{tr} \tilde{\boldsymbol{s}}^{\mathrm{p}} \leq \sqrt{\frac{2}{3}} (A_\theta - A_\varphi) \operatorname{tr} \boldsymbol{s}^{\mathrm{p}} \right\}. \tag{57}$$

Employing a result of Laborde [125, Proposition 4] (see also Francfort [110] and references therein), we then recover the generalized stress constraint (55) and the non-associative flow rule (56) as the necessary conditions of the *generalized principle of maximum dissipation* [105], defined here for all $\dot{\boldsymbol{\varepsilon}}^{\mathrm{p}} \in \mathbb{R}^{3\times 3}_{\mathrm{sym}}$ as

$$\phi^{\mathrm{p}}(\dot{\boldsymbol{\varepsilon}}^{\mathrm{p}}; \boldsymbol{s}^{\mathrm{p}}) = \sup\left\{ \tilde{\boldsymbol{s}}^{\mathrm{p}} : \dot{\boldsymbol{\varepsilon}}^{\mathrm{p}} - I_{\mathbb{L}(\boldsymbol{s}^{\mathrm{p}})}(\tilde{\boldsymbol{s}}^{\mathrm{p}}) \right\}, \tag{58}$$

where $I_\square$ is the indicator function of a convex set $\square$. A consequence of non-associativity is that the dissipation potential $\phi^{\mathrm{p}}(\dot{\boldsymbol{\varepsilon}}^{\mathrm{p}}; \boldsymbol{s}^{\mathrm{p}})$ inherits the dependence on the generalized stress $\boldsymbol{s}^{\mathrm{p}}$. Evaluating the supremum (58) yields the plastic dissipation potential [83]

$$\phi^{\mathrm{p}}(\dot{\boldsymbol{\varepsilon}}^{\mathrm{p}}; \boldsymbol{s}^{\mathrm{p}}) = \begin{cases} \dfrac{\operatorname{tr} \dot{\boldsymbol{\varepsilon}}^{\mathrm{p}}}{3A_\theta} (A_\theta - A_\varphi) \operatorname{tr} \boldsymbol{s}^{\mathrm{p}} & \text{if } \operatorname{tr} \dot{\boldsymbol{\varepsilon}}^{\mathrm{p}} \geq \sqrt{6} A_\theta \|\dot{\boldsymbol{\varepsilon}}^{\mathrm{p}}_{\mathrm{dev}}\|, \\ +\infty \quad \text{otherwise.} \end{cases} \tag{59}$$

Note that for $A_\theta = A_\varphi$, the plastic dissipation potential vanishes, rendering the associative model inconsistent with the dissipative frictional nature of $\boldsymbol{\varepsilon}^{\mathrm{p}}$ and thus highlighting a crucial role of non-associativity.

On the other hand, the fracture contribution to the dissipation potential (53) is defined as an extension of conventional phase-field models [58, 116] to account for the distinction between mode I fracture in the tensile regime and mode II fracture in the compressive/shear regime. Specifically, we define

$$\phi^{\mathrm{d}}(\dot{\alpha}, \nabla\dot{\alpha}; \alpha, \nabla\alpha, \boldsymbol{s}^{\mathrm{p}}) \coloneqq \begin{cases} \dfrac{G_{\mathrm{c}}(\boldsymbol{s}^{\mathrm{p}})}{\ell} \big(\alpha\, \dot{\alpha} + \ell^2 \nabla\alpha \cdot \nabla\dot{\alpha} \big) & \text{if } \dot{\alpha} \geq 0, \\ +\infty \quad \text{otherwise,} \end{cases} \quad \text{with} \quad G_{\mathrm{c}}(\boldsymbol{s}^{\mathrm{p}}) \coloneqq \begin{cases} G_{\mathrm{cI}} & \text{if } \operatorname{tr} \boldsymbol{s}^{\mathrm{p}} = 0, \\ G_{\mathrm{cII}} & \text{if } \operatorname{tr} \boldsymbol{s}^{\mathrm{p}} < 0, \end{cases} \tag{60}$$

where ℓ is the fracture length scale. The damage irreversibility condition $\dot{\alpha} \geq 0$ is automatically enforced in this definition. Moreover, fracture in the tensile regime and fracture in the compressive/shear regime are governed by the mode I fracture toughness G_{cI} and the mode II fracture toughness G_{cII}, respectively. This feature of the model plays a crucial role in capturing different failure modes including mixed-mode fracture, as thoroughly discussed for the dry case in Ulloa et al. [83].

Convective dissipation. It is left to define the convective dissipation potential that characterizes the resistance to fluid flow. With the variational principle (25) in mind, and in agreement with equation (13), the dual convective dissipation potential reads

$$\phi^{\star}_{\mathrm{con}}(-\nabla p; \boldsymbol{\varepsilon}, \alpha, \nabla\alpha) = \frac{1}{2} \boldsymbol{K}(\boldsymbol{\varepsilon}, \alpha, \nabla\alpha) : (-\nabla p \otimes -\nabla p). \tag{61}$$

The Darcy-type law then follows from (13) as

$$\boldsymbol{h} = -\frac{\partial}{\partial \nabla p}\phi^{\star}_{\mathrm{con}}(-\nabla p; \boldsymbol{\varepsilon}, \alpha, \nabla\alpha) = -\boldsymbol{K}(\boldsymbol{\varepsilon}, \alpha, \nabla\alpha)\cdot\nabla p. \tag{62}$$

Here, the permeability tensor $\boldsymbol{K}$ is adopted from Mauthe and Miehe [98], where a transition is assumed between Darcy flow in the unfractured material points and Poiseuille flow along macroscopic cracks, i.e., where $\alpha(\boldsymbol{x}, t) = 1$ (figure 3). To this end, the anisotropic permeability tensor

$$\boldsymbol{K}(\boldsymbol{\varepsilon}, \alpha, \nabla\alpha) \coloneqq \frac{K_{\mathrm{D}}}{\eta_{\mathrm{vf}}}\mathbf{1} + \frac{\alpha^{\epsilon}}{\eta_{\mathrm{vf}}}\big(w_{\alpha}(\boldsymbol{\varepsilon}, \nabla\alpha)^2 - K_{\mathrm{D}}\big)\big(\mathbf{1} - \boldsymbol{n}_{\alpha}\otimes\boldsymbol{n}_{\alpha}\big) \tag{63}$$

is considered, where $\epsilon > 1$ is an interpolation parameter. The first term represents the contribution of isotropic Darcy permeability, where K_{D} is the permeability constant and η_{vf} is the viscosity of the fluid. The second term accounts for enhanced permeability along a macroscopic crack whose normal direction is given by the vector $\boldsymbol{n}_{\alpha} \approx \nabla\alpha/\|\nabla\alpha\|$. We note that this expression is an approximation of the normal direction that has been successfully employed in the phase-field literature for hydraulic fracture as well as in anisotropic fracture models [126]. Moreover, in equation (63), w_{α} denotes an estimation of the crack aperture, computed from the kinematics as the scalar quantity $w_{\alpha} = h_{\mathrm{c}}\boldsymbol{n}_{\alpha}\cdot\boldsymbol{\varepsilon}\cdot\boldsymbol{n}_{\alpha}$; here h_{c} is the characteristic finite element size along the direction $\boldsymbol{n}_{\alpha}$ in a fractured element line.

The evaluation of the permeability tensor (63) is heuristic, particularly concerning the estimation of the crack opening w_{α} and the crack normal direction $\boldsymbol{n}_{\alpha}$. This standard choice is made for the sake of simplicity, in agreement with several works [95, 98–100, 103]. Nevertheless, although the contribution of the second term in equation (63) only becomes significant as $\alpha \to 1$, i.e., at fully developed cracks, it must be mentioned that the estimation of the crack opening suffers from mesh sensitivity at fully fractured states [86, 103], and that the estimation of the crack normal direction is not consistent at the crack tip [127]. Improvements to overcome these limitations have been proposed in the literature [86, 127, 128]. In the present work, such improvements can be applied at this point, but are not pursued since we have mainly focused on the coupling between fluid flow and the micromechanics-based characterization of brittle and ductile failure.

At this point, the constitutive energy functions of the model have been established in terms of the free energy density (44) and the dissipation potentials (59), (60), and (61). These functions constitute the building blocks of the variational formulation presented below.

3.2.3. Variational formulation and governing equations

The variational formulation of the proposed model in terms of the saddle-point principle (25) requires the definition of the following function spaces:

$$\dot{\mathscr{U}} \coloneqq \{\boldsymbol{w}\in\mathrm{BD}(\Omega;\mathbb{R}^3) \;\mid\; \boldsymbol{w} = \dot{\bar{\boldsymbol{u}}} \text{ on } \Gamma^{u}_{\mathrm{D}}\}, \qquad \tilde{\mathscr{U}} \coloneqq \{\boldsymbol{w}\in\mathrm{BD}(\Omega;\mathbb{R}^3) \;\mid\; \boldsymbol{w} = \boldsymbol{0} \text{ on } \Gamma^{u}_{\mathrm{D}}\}, \tag{64}$$

$$\mathscr{P} \coloneqq \{q\in\mathrm{H}^1(\Omega) \;\mid\; q = \bar{p} \text{ on } \Gamma^{p}_{\mathrm{D}}\}, \qquad \tilde{\mathscr{P}} \coloneqq \{q\in\mathrm{H}^1(\Omega) \;\mid\; q = 0 \text{ on } \Gamma^{p}_{\mathrm{D}}\}, \tag{65}$$

$$\dot{\mathscr{Z}} \coloneqq \mathrm{L}^2(\Omega), \tag{66}$$

$$\dot{\mathscr{B}} \coloneqq \{\boldsymbol{e}\in\mathrm{M_b}(\Omega\cup\Gamma_{\mathrm{D}};\mathbb{R}^{3\times3}_{\mathrm{sym}}) \;\mid\; \operatorname{tr}\boldsymbol{e} \geq \sqrt{6}A_{\theta}\|\boldsymbol{e}_{\mathrm{dev}}\|\}, \tag{67}$$

$$\dot{\mathscr{D}} \coloneqq \mathrm{H}^1(\Omega;\mathbb{R}_+). \tag{68}$$

Here, we have employed the space of bounded deformations BD and the space of Radon measures $\mathrm{M_b}$ in view of the perfect plasticity state that can be attained in the compressive/shear regime as $\alpha \to 1$ (see

equations (43), (47), and (54)), resulting in plastic strain localization. We refer the reader to the recent work of Crismale [129] for the mathematical treatment of a similar model in the context of dry materials. Note that equations (67) and (68) embed the constraints present in the dissipation potentials (59) and (60), such that the global dissipative power (17) remains finite. As such, only non-trivial conditions that fulfill the first-order stability condition (21) are considered.

With the function spaces above, and replacing the energy densities defined in sections 3.2.1 and 3.2.2 in the global energy functionals (14), (17), and (24), the saddle-point principle (25) takes the form

$$\inf_{\dot{\boldsymbol{u}}\in\dot{\mathscr{U}}}\inf_{\dot{\boldsymbol{\varepsilon}}^{\mathrm{p}}\in\dot{\mathscr{B}}}\inf_{\dot{\alpha}\in\dot{\mathscr{D}}}\inf_{\dot{\zeta}\in\dot{\mathscr{Z}}}\sup_{p\in\mathscr{P}}\Bigg\{\int_\Omega\Bigg(\frac{\partial\psi}{\partial\boldsymbol{\varepsilon}}:\nabla^{\mathrm{s}}\dot{\boldsymbol{u}}+\frac{\partial\psi}{\partial\zeta}\,\dot{\zeta}+\frac{\partial\psi}{\partial\boldsymbol{\varepsilon}^{\mathrm{p}}}:\dot{\boldsymbol{\varepsilon}}^{\mathrm{p}}+\frac{\partial\psi}{\partial\alpha}\,\dot{\alpha}-p\,\dot{\zeta}-\frac{1}{2}\boldsymbol{K}(\boldsymbol{\varepsilon},\alpha,\nabla\alpha):(\nabla p\otimes\nabla p)$$
$$+\frac{\operatorname{tr}\dot{\boldsymbol{\varepsilon}}^{\mathrm{p}}}{3A_\theta}(A_\theta-A_\varphi)\operatorname{tr}\boldsymbol{s}^{\mathrm{p}}+\frac{G_{\mathrm{c}}(\boldsymbol{s}^{\mathrm{p}})}{\ell}\big(\alpha\,\dot{\alpha}+\ell^2\nabla\alpha\cdot\nabla\dot{\alpha}\big)\Bigg)\mathrm{d}\boldsymbol{x}-\mathcal{P}^u(t,\dot{\boldsymbol{u}})-\mathcal{P}^p(t,p)\Bigg\}. \tag{69}$$

The governing equations directly follow from (69) as described below.

Mechanical balance. Taking variations of the objective functional in (69) with respect to $\dot{\boldsymbol{u}}$ yields

$$\int_\Omega\big(\boldsymbol{\sigma}:\nabla^{\mathrm{s}}\tilde{\boldsymbol{u}}-\rho\boldsymbol{b}\cdot\tilde{\boldsymbol{u}}\big)\,\mathrm{d}\boldsymbol{x}-\int_{\Gamma_{\mathrm{N}}^u}\bar{\boldsymbol{t}}\cdot\tilde{\boldsymbol{u}}\,\mathrm{d}S=0\quad\forall\,\tilde{\boldsymbol{u}}\in\tilde{\mathscr{U}}, \tag{70}$$

with $\boldsymbol{\sigma}$ given in equation (45), recovering the weak form of the equilibrium equations (1).

Fluid balance. Taking variations of the objective functional in (69) with respect to $\dot{\zeta}$ yields, for all admissible test functions $\tilde{\zeta}\in\dot{\mathscr{Z}}$, the local constitutive relation between p and ζ, i.e., equation (46).

On the other hand, taking variations with respect to p yields

$$\int_\Omega\Big(-\dot{\zeta}\,\tilde{p}-\nabla p\cdot\boldsymbol{K}(\boldsymbol{\varepsilon},\alpha,\nabla\alpha)\cdot\nabla\tilde{p}\Big)\,\mathrm{d}\boldsymbol{x}-\int_{\Gamma_{\mathrm{N}}^p}\bar{h}\,\tilde{p}\,\mathrm{d}S=0\quad\forall\,\tilde{p}\in\tilde{\mathscr{P}}, \tag{71}$$

recovering the weak form of the fluid balance equations (2).

Plasticity evolution equations. In agreement with the derivations of previous works [83, 105], taking variations of the objective functional in (69) with respect to $\dot{\boldsymbol{\varepsilon}}^{\mathrm{p}}$ yields the bulk condition

$$\boldsymbol{s}^{\mathrm{p}}\in\frac{1}{3A_\theta}(A_\theta-A_\varphi)\operatorname{tr}\boldsymbol{s}^{\mathrm{p}}\mathbf{1}+\partial I_{\mathbb{R}_+}\big(\operatorname{tr}\dot{\boldsymbol{\varepsilon}}^{\mathrm{p}}-\sqrt{6}A_\theta\|\dot{\boldsymbol{\varepsilon}}^{\mathrm{p}}_{\mathrm{dev}}\|\big)\equiv\partial_1\phi^{\mathrm{p}}(\dot{\boldsymbol{\varepsilon}}^{\mathrm{p}};\boldsymbol{s}^{\mathrm{p}}), \tag{72}$$

with $\boldsymbol{s}^{\mathrm{p}}$ given in equation (47). Here, the indicator function accounts for the conic constraint in the dissipation potential (59), embedded in the function space (67), and $\partial_1\phi(\square;\bullet)$ denotes the subdifferential of ϕ with respect to $\square$. This expression is a primal representation of the plasticity evolution equations (cf. [105, 110])

$$f^{\mathrm{p}}(\boldsymbol{s}^{\mathrm{p}})\leq 0,\quad\lambda\geq 0,\quad\lambda\,f^{\mathrm{p}}(\boldsymbol{s}^{\mathrm{p}})=0 \tag{73}$$

and

$$\dot{\boldsymbol{\varepsilon}}^{\mathrm{p}}=\lambda\,\hat{\boldsymbol{n}},\quad\hat{\boldsymbol{n}}\in\partial g^{\mathrm{p}}(\boldsymbol{s}^{\mathrm{p}})=\partial\|\boldsymbol{s}^{\mathrm{p}}_{\mathrm{dev}}\|+\sqrt{2/3}\,A_\theta\mathbf{1}. \tag{74}$$

Thus, we recover the generalized stress constraint (55) and the non-associative flow rule (56).

Damage evolution equations. Finally, taking variations of equation (69) with respect to $\dot{\alpha}$ gives

$$\int_\Omega \Big(- s^{\mathrm{d}}\,\tilde{\alpha} + \frac{G_{\mathrm{c}}(\boldsymbol{s}^{\mathrm{p}})}{\ell}\big(\alpha\,\tilde{\alpha} + \ell^2 \nabla\alpha\cdot\nabla\tilde{\alpha}\big) + I_{\mathbb{R}_+}(\dot{\alpha})\,\tilde{\alpha}\Big)\,\mathrm{d}\boldsymbol{x} \ni 0 \quad \forall\,\tilde{\alpha}\in \mathrm{H}^1(\Omega;\mathbb{R}), \tag{75}$$

where the indicator function accounts for the irreversibility constraint in the dissipation potential (60), embedded in the function space (68). After integrating by parts, we recover the conditions

$$f^{\mathrm{d}}(s^{\mathrm{d}};\boldsymbol{s}^{\mathrm{p}}) \le 0, \quad \dot{\alpha}\ge 0, \quad \dot{\alpha}\, f^{\mathrm{d}}(s^{\mathrm{d}};\boldsymbol{s}^{\mathrm{p}}) = 0 \quad \text{in } \Omega, \qquad \text{and} \qquad \nabla\alpha\cdot\boldsymbol{n} = 0 \quad \text{on } \Gamma, \tag{76}$$

where the damage yield function reads

$$f^{\mathrm{d}}(s^{\mathrm{d}};\boldsymbol{s}^{\mathrm{p}}) := s^{\mathrm{d}} - \frac{G_{\mathrm{c}}(\boldsymbol{s}^{\mathrm{p}})}{\ell}\alpha + \ell\,\mathrm{div}[G_{\mathrm{c}}(\boldsymbol{s}^{\mathrm{p}})\nabla\alpha]. \tag{77}$$

Finally, for post-processing purposes, we define the equivalent plastic strain in the compressive/shear regime as a measure of frictional sliding:

$$\dot{\kappa} := \begin{cases} 0 & \text{if } \operatorname{tr}\boldsymbol{s}^{\mathrm{p}} = 0 \quad (\textsf{open}),\\ \sqrt{2/3}\,\|\dot{\boldsymbol{\varepsilon}}^{\mathrm{p}}\| & \text{if } \operatorname{tr}\boldsymbol{s}^{\mathrm{p}} < 0 \quad (\textsf{closed}). \end{cases} \tag{78}$$

Table 1. Energy quantities and state equations.

Free energy and state equations	
Stored energy	$\psi(\boldsymbol{\varepsilon},\zeta,\boldsymbol{\varepsilon}^{\mathrm{p}},\alpha) = \begin{cases} \frac{1}{2}\,\boldsymbol{\varepsilon}:\mathbf{C}^{\mathrm{dam}}(\alpha):\boldsymbol{\varepsilon} + \frac{M^{\mathrm{dam}}(\alpha)}{2}\big(B^{\mathrm{dam}}(\alpha)\operatorname{tr}\boldsymbol{\varepsilon}-\zeta\big)^2 & \text{if open},\\ \frac{1}{2}(\boldsymbol{\varepsilon}-\boldsymbol{\varepsilon}^{\mathrm{p}}):\mathbf{C}:(\boldsymbol{\varepsilon}-\boldsymbol{\varepsilon}^{\mathrm{p}}) + \frac{1}{2}\,\boldsymbol{\varepsilon}^{\mathrm{p}}:\mathbf{H}^{\mathrm{kin}}(\alpha):\boldsymbol{\varepsilon}^{\mathrm{p}} & \\ \qquad + \frac{M}{2}\big[B\operatorname{tr}(\boldsymbol{\varepsilon}-\boldsymbol{\varepsilon}^{\mathrm{p}}) - (\zeta-\operatorname{tr}\boldsymbol{\varepsilon}^{\mathrm{p}})\big]^2 & \text{if closed} \end{cases}$
Generalized stresses	$\boldsymbol{\sigma}(\boldsymbol{\varepsilon},\zeta,\boldsymbol{\varepsilon}^{\mathrm{p}},\alpha) = \frac{\partial\psi}{\partial\boldsymbol{\varepsilon}}, \qquad \boldsymbol{s}^{\mathrm{p}}(\boldsymbol{\varepsilon},\zeta,\boldsymbol{\varepsilon}^{\mathrm{p}},\alpha) = -\frac{\partial\psi}{\partial\boldsymbol{\varepsilon}^{\mathrm{p}}},$ $p(\boldsymbol{\varepsilon},\zeta,\boldsymbol{\varepsilon}^{\mathrm{p}},\alpha) = \frac{\partial\psi}{\partial\zeta}, \qquad s^{\mathrm{d}}(\boldsymbol{\varepsilon},\zeta,\boldsymbol{\varepsilon}^{\mathrm{p}},\alpha) = -\frac{\partial\psi}{\partial\alpha}$
Opening/closure transition	$\begin{cases} \operatorname{tr}\boldsymbol{s}^{\mathrm{p}}(\boldsymbol{\varepsilon},\zeta,\boldsymbol{\varepsilon}^{\mathrm{p}},\alpha) = 0 & \text{if open},\\ \operatorname{tr}\boldsymbol{s}^{\mathrm{p}}(\boldsymbol{\varepsilon},\zeta,\boldsymbol{\varepsilon}^{\mathrm{p}},\alpha) < 0 & \text{if closed} \end{cases}$
Intrinsic dissipation potential: $\phi_{\mathrm{int}} = \phi^{\mathrm{p}} + \phi^{\mathrm{d}} \ge 0$	
Plastic dissipation potential	$\phi^{\mathrm{p}}(\dot{\boldsymbol{\varepsilon}}^{\mathrm{p}};\boldsymbol{s}^{\mathrm{p}}) = \begin{cases} \frac{\operatorname{tr}\dot{\boldsymbol{\varepsilon}}^{\mathrm{p}}}{3A_\theta}(A_\theta - A_\varphi)\operatorname{tr}\boldsymbol{s}^{\mathrm{p}} & \text{if } \operatorname{tr}\dot{\boldsymbol{\varepsilon}}^{\mathrm{p}} \ge \sqrt{6}A_\theta\|\dot{\boldsymbol{\varepsilon}}^{\mathrm{p}}_{\mathrm{dev}}\|,\\ +\infty \quad \text{otherwise} \end{cases}$
Damage dissipation potential	$\phi^{\mathrm{d}}(\dot{\alpha},\nabla\dot{\alpha};\alpha,\nabla\alpha,\boldsymbol{s}^{\mathrm{p}}) = \begin{cases} \frac{G_{\mathrm{c}}(\boldsymbol{s}^{\mathrm{p}})}{\ell}\big(\alpha\,\dot{\alpha} + \ell^2\nabla\alpha\cdot\nabla\dot{\alpha}\big) & \text{if } \dot{\alpha}\ge 0,\\ +\infty \quad \text{otherwise} \end{cases}$
Convective dissipation potential: $\phi^{\star}_{\mathrm{con}} \ge 0$	
Dual fluid dissipation potential	$\phi^{\star}_{\mathrm{con}}(-\nabla p;\boldsymbol{\varepsilon},\alpha,\nabla\alpha) = \frac{1}{2}\boldsymbol{K}(\boldsymbol{\varepsilon},\alpha,\nabla\alpha):(-\nabla p\otimes -\nabla p)$
Darcy-Poiseuille law	$\boldsymbol{h} = -\frac{\partial}{\partial\nabla p}\phi^{\star}_{\mathrm{con}}(-\nabla p;\boldsymbol{\varepsilon},\alpha,\nabla\alpha)$

Overview. At this point, we have obtained the governing equations of the multiphysics coupled system, consisting of mechanical balance, fluid balance, the plasticity evolution problem, and the damage evolution problem. Depending on the opening/closure transition (48), the model can be viewed as a modified brittle phase-field model coupled to poroelasticity (tensile regime) or as a ductile damage model coupled to poroplasticity, where fracture is only driven by plastic strains (compressive/shear regime). At the microcrack level, the former is associated with opening microcracks, while the latter is associated with a coupling between microcrack growth and frictional sliding. Tables 1 and 2 present an overview of the proposed model.

Table 2. Governing equations according to the energetic formulation.

Kinematic admissibility	
Infinitesimal strain	$\boldsymbol{\varepsilon}(\boldsymbol{u}) = \nabla^{\mathrm{s}}\boldsymbol{u}$
Dirichlet boundary condition	$\boldsymbol{u} = \bar{\boldsymbol{u}}$ on Γ_{D}^{u}
Pore pressure admissibility	
Dirichlet boundary condition	$p = \bar{p}$ on Γ_{D}^{p}
Mechanical balance	
Stress	$\boldsymbol{\sigma}(\boldsymbol{\varepsilon}, p, \boldsymbol{\varepsilon}^{\mathrm{p}}, \alpha) = \begin{cases} \mathbf{C}^{\mathrm{dam}}(\alpha) : \boldsymbol{\varepsilon} - B^{\mathrm{dam}}(\alpha)\, p\mathbf{1} & \text{if } \operatorname{tr}\boldsymbol{s}^{\mathrm{p}} = 0 \quad (\mathsf{open}), \\ \mathbf{C} : (\boldsymbol{\varepsilon} - \boldsymbol{\varepsilon}^{\mathrm{p}}) - B\, p\mathbf{1} & \text{if } \operatorname{tr}\boldsymbol{s}^{\mathrm{p}} < 0 \quad (\mathsf{closed}) \end{cases}$
Equilibrium	$\operatorname{div}\boldsymbol{\sigma}(\boldsymbol{\varepsilon}, p, \boldsymbol{\varepsilon}^{\mathrm{p}}, \alpha) + \rho\boldsymbol{b} = \mathbf{0}$ in Ω
Neumann boundary condition	$\boldsymbol{\sigma}(\boldsymbol{\varepsilon}, p, \boldsymbol{\varepsilon}^{\mathrm{p}}, \alpha) \cdot \boldsymbol{n} = \bar{\boldsymbol{t}}$ on Γ_{N}^{u}
Fluid balance	
Pressure	$p(\boldsymbol{\varepsilon}, \zeta, \boldsymbol{\varepsilon}^{\mathrm{p}}, \alpha) = \begin{cases} -M^{\mathrm{dam}}(\alpha)(B^{\mathrm{dam}}(\alpha)\operatorname{tr}\boldsymbol{\varepsilon} - \zeta) & \text{if } \operatorname{tr}\boldsymbol{s}^{\mathrm{p}} = 0 \quad (\mathsf{open}), \\ -M\big[B\operatorname{tr}(\boldsymbol{\varepsilon} - \boldsymbol{\varepsilon}^{\mathrm{p}}) - (\zeta - \operatorname{tr}\boldsymbol{\varepsilon}^{\mathrm{p}})\big] & \text{if } \operatorname{tr}\boldsymbol{s}^{\mathrm{p}} < 0 \quad (\mathsf{closed}) \end{cases}$
Flux	$\boldsymbol{h} = -\boldsymbol{K}(\boldsymbol{\varepsilon}, \alpha, \nabla\alpha) \cdot \nabla p$
Fluid flow	$\dot{\zeta} + \operatorname{div}\boldsymbol{h} = 0$ in Ω
Neumann boundary condition	$\boldsymbol{h} \cdot \boldsymbol{n} = \bar{h}$ on Γ_{N}^{p}
Plasticity evolution problem	
Generalized stress	$\boldsymbol{s}^{\mathrm{p}}(\boldsymbol{\varepsilon}, p, \boldsymbol{\varepsilon}^{\mathrm{p}}, \alpha) = \mathbf{C} : (\boldsymbol{\varepsilon} - \boldsymbol{\varepsilon}^{\mathrm{p}}) - \mathbf{H}^{\mathrm{kin}}(\alpha) : \boldsymbol{\varepsilon}^{\mathrm{p}} - B\, p\mathbf{1} + p\mathbf{1}$
Yield function	$f^{\mathrm{p}}(\boldsymbol{s}^{\mathrm{p}}) = \lVert\boldsymbol{s}_{\mathrm{dev}}^{\mathrm{p}}\rVert + \sqrt{2/3}\, A_{\varphi}\operatorname{tr}\boldsymbol{s}^{\mathrm{p}}$
Plastic potential	$g^{\mathrm{p}}(\boldsymbol{s}^{\mathrm{p}}) = \lVert\boldsymbol{s}_{\mathrm{dev}}^{\mathrm{p}}\rVert + \sqrt{2/3}\, A_{\theta}\operatorname{tr}\boldsymbol{s}^{\mathrm{p}}$
KKT system	$f^{\mathrm{p}}(\boldsymbol{s}^{\mathrm{p}}) \le 0, \quad \lambda \ge 0, \quad \lambda\, f^{\mathrm{p}}(\boldsymbol{s}^{\mathrm{p}}) = 0$
Flow rule	$\dot{\boldsymbol{\varepsilon}}^{\mathrm{p}} = \lambda\, \hat{\boldsymbol{n}}, \quad \hat{\boldsymbol{n}} \in \partial g^{\mathrm{p}}(\boldsymbol{s}^{\mathrm{p}}) = \partial\lVert\boldsymbol{s}_{\mathrm{dev}}^{\mathrm{p}}\rVert + \sqrt{2/3}\, A_{\theta}\mathbf{1}$
Damage evolution problem	
Generalized stress	$s^{\mathrm{d}}(\boldsymbol{\varepsilon}, p, \boldsymbol{\varepsilon}^{\mathrm{p}}, \alpha) = \begin{cases} -\dfrac{1}{2K}\, g_K'(\alpha)\,(K\operatorname{tr}\boldsymbol{\varepsilon} - Bp + p)^2 & \\ \qquad\qquad -g_\mu'(\alpha)\,\mu\,\boldsymbol{\varepsilon}_{\mathrm{dev}} : \boldsymbol{\varepsilon}_{\mathrm{dev}} & \text{if } \operatorname{tr}\boldsymbol{s}^{\mathrm{p}} = 0 \quad (\mathsf{open}), \\ -\dfrac{1}{2}\, H_K^{\mathrm{kin}\prime}(\alpha)(\operatorname{tr}\boldsymbol{\varepsilon}^{\mathrm{p}})^2 - \dfrac{1}{2}\, H_\mu^{\mathrm{kin}\prime}(\alpha)\, \boldsymbol{\varepsilon}_{\mathrm{dev}}^{\mathrm{p}} : \boldsymbol{\varepsilon}_{\mathrm{dev}}^{\mathrm{p}} & \text{if } \operatorname{tr}\boldsymbol{s}^{\mathrm{p}} < 0 \quad (\mathsf{closed}) \end{cases}$
Yield function	$f^{\mathrm{d}}(s^{\mathrm{d}}; \boldsymbol{s}^{\mathrm{p}}) = s^{\mathrm{d}} - \dfrac{G_{\mathrm{c}}(\boldsymbol{s}^{\mathrm{p}})}{\ell}\alpha + \ell\operatorname{div}[G_{\mathrm{c}}(\boldsymbol{s}^{\mathrm{p}})\nabla\alpha]$
KKT system	$f^{\mathrm{d}}(s^{\mathrm{d}}; \boldsymbol{s}^{\mathrm{p}}) \le 0, \quad \dot{\alpha} \ge 0, \quad \dot{\alpha}\, f^{\mathrm{d}}(s^{\mathrm{d}}; \boldsymbol{s}^{\mathrm{p}}) = 0 \quad \text{in } \Omega$
Boundary condition	$\nabla\alpha \cdot \boldsymbol{n} = 0$ on Γ

4. Numerical implementation

Let us now discuss the main aspects of the numerical implementation of the evolution equations summarized in table 2. We consider a time discretization $0 = t_0 < \cdots < t_n < t_{n+1} < \cdots < t_{n_t} = t_{\max}$, where all quantities are known up to t_n, and the goal is to find the state at the current time step t_{n+1}. We denote a quantity $\square$ evaluated at the previous time step t_n as $\square_n$, while a quantity evaluated at t_{n+1} is written without a subscript, i.e., $\square \coloneqq \square_{n+1}$. Moreover, $\Delta\square \coloneqq \square - \square_n$ denotes an increment of $\square$ from t_n to t_{n+1}.

In order to incorporate the effect of fluid flow, the numerical implementation of the present model follows a straightforward extension of the procedure described in detail in Ulloa et al. [83]. Therefore, for the sake of brevity, only the new features are emphasized in the sequel and the reader is referred to Ulloa et al. [83, section 3] for details on the reference procedure.

4.1. Staggered algorithm

In order to solve the multiphysics coupled system, an algorithmic decoupling is employed by means of a semi-staggered scheme. Therein, the elastoplastic problem, the fluid balance problem, and the damage problem are iteratively solved for $\{\boldsymbol{u}, \boldsymbol{\varepsilon}^{\mathrm{p}}\}$, p, and α, respectively. Therefore, the scheme resembles the iterative split often employed in poromechanics [130], hereby extended to elastoplasticity and fracture. The solution procedure is summarized in algorithm 1.

Algorithm 1. The staggered solution procedure.

Input: primary fields at the previous time step $\boldsymbol{u}_n$, $\boldsymbol{\varepsilon}^{\mathrm{p}}_n$, p_n, and α_n.

Output: primary fields at the current time step $\boldsymbol{u}$, $\boldsymbol{\varepsilon}^{\mathrm{p}}$, p, and α.

1: Initialize iterations with $j \coloneqq 0$ and $\{\boldsymbol{u}^{(0)}, \boldsymbol{\varepsilon}^{\mathrm{p}(0)}, p^{(0)}, \alpha^{(0)}\} \coloneqq \{\boldsymbol{u}_n, p_n\, \boldsymbol{\varepsilon}^{\mathrm{p}}_n, \alpha_n\}$.

2: **repeat**

3: Set $j \leftarrow j + 1$.

4: Solve the non-linear elastoplastic problem for $\{\boldsymbol{u}^{(j)}, \boldsymbol{\varepsilon}^{\mathrm{p}(j)}\}$ using $\{p^{(j-1)}, \alpha^{(j-1)}\}$ (section 4.2).

5: Solve the linear fluid balance problem for $p^{(j)}$ using $\{\boldsymbol{u}^{(j)}, \boldsymbol{\varepsilon}^{\mathrm{p}(j)}, \alpha^{(j-1)}\}$ (section 4.3).

6: Solve the non-linear damage problem for $\alpha^{(j)}$ using $\{\boldsymbol{u}^{(j)}, \boldsymbol{\varepsilon}^{\mathrm{p}(j)}, p^{(j)}\}$ (section 4.4).

7: Update

$$\mathtt{RES}^{(j)}_{\mathrm{stag}} \coloneqq \int_\Omega \Big[\boldsymbol{\sigma}\big(\nabla^{\mathrm{s}}\boldsymbol{u}^{(j)}, p^{(j)}, \boldsymbol{\varepsilon}^{\mathrm{p}(j)}, \alpha^{(j)}\big) : \nabla^{\mathrm{s}}\tilde{\boldsymbol{u}} - \rho\boldsymbol{b}\cdot\tilde{\boldsymbol{u}}\Big]\,\mathrm{d}\boldsymbol{x} - \int_{\Gamma^u_{\mathrm{N}}} \bar{\boldsymbol{t}}\cdot\tilde{\boldsymbol{u}}\,\mathrm{d}S \quad \forall\,\tilde{\boldsymbol{u}} \in \tilde{\mathscr{U}}.$$

8: **until** $\big|\mathtt{RES}^{(j)}_{\mathrm{stag}}\big| \leq \mathtt{TOL}_{\mathrm{stag}}$.

9: Set $\{\boldsymbol{u}, \boldsymbol{\varepsilon}^{\mathrm{p}}, p, \alpha\} \coloneqq \{\boldsymbol{u}^{(j)}, \boldsymbol{\varepsilon}^{\mathrm{p}(j)}, p^{(j)}, \alpha^{(j)}\}$.

4.2. Elastoplastic evolution problem

According to algorithm 1, the task of finding $\{\boldsymbol{u}, \boldsymbol{\varepsilon}^{\mathrm{p}}\}$ with fixed $\{\alpha, p\}$ can be viewed as a classical non-linear elastoplasticity problem, where the plastic strains evolve according to a non-cohesive Drucker-Prager model with kinematic hardening. This problem is solved by linearizing the mechanical balance equation

$$\int_\Omega \big(\boldsymbol{\sigma}(\boldsymbol{\varepsilon}, p, \boldsymbol{\varepsilon}^{\mathrm{p}}, \alpha) : \nabla^{\mathrm{s}}\tilde{\boldsymbol{u}} - \rho\boldsymbol{b}\cdot\tilde{\boldsymbol{u}}\big)\,\mathrm{d}\boldsymbol{x} - \int_{\Gamma^u_{\mathrm{N}}} \bar{\boldsymbol{t}}\cdot\tilde{\boldsymbol{u}}\,\mathrm{d}S = 0 \quad \forall\,\tilde{\boldsymbol{u}} \in \tilde{\mathscr{U}} \tag{79}$$

and updating the plastic strain tensor $\boldsymbol{\varepsilon}^{\mathrm{p}}$ via local return-mapping [131–133]. The procedure for the dry case, i.e., with $p = 0$, is presented in detail in Ulloa et al. [83]. In the present study, the effect of a non-vanishing p, known at this stage from the algorithmic decoupling, is readily incorporated into the procedure through the constitutive equations (50) and (51).

4.3. Fluid balance problem

According to algorithm 1, given $\{\boldsymbol{u}, \boldsymbol{\varepsilon}^{\mathrm{p}}, \alpha\}$, a linear fluid balance problem is solved in terms of the pore pressure p. To achieve this, we first invert equation (46) and compute

$$\dot{\zeta} = \begin{cases} \dfrac{\dot{p}}{M^{\mathrm{dam}}(\alpha)} + B^{\mathrm{dam}}(\alpha)\,\mathrm{tr}\,\dot{\boldsymbol{\varepsilon}} - \dfrac{1}{K}(1-B)g_K'(\alpha)(K\,\mathrm{tr}\,\boldsymbol{\varepsilon} - B\,p + p)\dot{\alpha} & \text{if } \mathsf{open}, \\ \dfrac{\dot{p}}{M} + B\,\mathrm{tr}\,\dot{\boldsymbol{\varepsilon}} + (1-B)\,\mathrm{tr}\,\dot{\boldsymbol{\varepsilon}}^{\mathrm{p}} & \text{if } \mathsf{closed}. \end{cases} \tag{80}$$

Note that this step can be skipped if the reduced saddle-point principle discussed in appendix A is directly employed. Introducing the temporal discretization described at the beginning of this section, we consider the incremental approximation $\dot{\zeta} \approx \Delta\zeta/\Delta t$, with

$$\Delta\zeta = \begin{cases} \dfrac{\Delta p}{M^{\mathrm{dam}}(\alpha)} + B^{\mathrm{dam}}(\alpha)\,\mathrm{tr}(\Delta\boldsymbol{\varepsilon}) - \dfrac{1}{K}(1-B)g_K'(\alpha)(K\,\mathrm{tr}\,\boldsymbol{\varepsilon} - B\,p + p)\Delta\alpha & \text{if } \mathsf{open}, \\ \dfrac{\Delta p}{M} + B\,\mathrm{tr}(\Delta\boldsymbol{\varepsilon}) + (1-B)\,\mathrm{tr}(\Delta\boldsymbol{\varepsilon}^{\mathrm{p}}) & \text{if } \mathsf{closed}. \end{cases} \tag{81}$$

Then, the incremental version of equation (71) takes the following linear form with p as the primary unknown:

$$\int_\Omega \Big(\Delta\zeta\,\tilde{p} + \Delta t\,\nabla p \cdot \boldsymbol{K}(\boldsymbol{\varepsilon}_n, \alpha_n, \nabla\alpha_n) \cdot \nabla\tilde{p} \Big)\,\mathrm{d}\boldsymbol{x} + \Delta t \int_{\Gamma_{\mathrm{N}}^p} \bar{h}\,\tilde{p}\,\mathrm{d}S = 0 \quad \forall\,\tilde{p} \in \tilde{\mathscr{P}}. \tag{82}$$

The permeability tensor is evaluated at the previous time step, in agreement with the numerical treatment of previous phase-field models for hydraulic fracture [98].

4.4. Damage evolution problem

According to algorithm 1, having determined $\{\boldsymbol{u}, \boldsymbol{\varepsilon}^{\mathrm{p}}, p\}$ at the current staggered iteration, we are now able to solve the damage evolution problem in order to update the crack phase-field α. Considering the incremental irreversibility condition $\Delta\alpha \geq 0$, the incremental version of equation (75) reads

$$\int_\Omega \Big(-s^{\mathrm{d}}(\boldsymbol{\varepsilon}, p, \boldsymbol{\varepsilon}^{\mathrm{p}}, \alpha)\,\tilde{\alpha} + \frac{G_{\mathrm{c}}(\boldsymbol{s}_n^{\mathrm{p}})}{\ell}\big(\alpha\,\tilde{\alpha} + \ell^2 \nabla\alpha \cdot \nabla\tilde{\alpha}\big) + \partial I_{\mathbb{R}_+}(\Delta\alpha)\,\tilde{\alpha} \Big)\,\mathrm{d}\boldsymbol{x} \ni 0 \quad \forall\,\tilde{\alpha} \in \mathrm{H}^1(\Omega;\mathbb{R}). \tag{83}$$

In order to resolve numerical instabilities related to brutal crack propagation, we consider a standard viscous regularization in the damage evolution problem [58], where a numerical damage viscosity parameter η_{vd} is introduced. This parameter must be chosen as small as possible to avoid significant deviations from the original problem. Equation (83) is then augmented as

$$\int_\Omega \Big(-s^{\mathrm{d}}(\boldsymbol{\varepsilon}, p, \boldsymbol{\varepsilon}^{\mathrm{p}}, \alpha)\,\tilde{\alpha} + \frac{G_{\mathrm{c}}(\boldsymbol{s}_n^{\mathrm{p}})}{\ell}\big(\alpha\,\tilde{\alpha} + \ell^2 \nabla\alpha \cdot \nabla\tilde{\alpha}\big) + \partial I_{\mathbb{R}_+}(\Delta\alpha) + \frac{\eta_{\mathrm{vd}}}{\Delta t}(\Delta\alpha)\,\tilde{\alpha} \Big)\,\mathrm{d}\boldsymbol{x} \ni 0 \quad \forall\,\tilde{\alpha} \in \mathrm{H}^1(\Omega;\mathbb{R}). \tag{84}$$

The adopted solution procedure for equation (84) consists of the following sequential steps: (i) evaluating the damage driving force s^{d} in terms of $\boldsymbol{s}^{\mathrm{p}}\big(\boldsymbol{\varepsilon}^{(j)}, p^{(j)}, \boldsymbol{\varepsilon}^{\mathrm{p}(j)}, \alpha^{(j-1)}\big)$, i.e., by assuming that the opening/closure

transition (48) is known from the solution of the elastoplastic problem and the pressure problem; (ii) adopting an extension of the *history field* approach [58] to handle the irreversibility constraint $\Delta\alpha \geq 0$ and render the inclusion (84) an equality; and (iii) employing a standard Newton-Raphson linearization to handle the non-linear terms in the driving force (52). The numerical solution procedure for the dry case, i.e., with $p = 0$, is presented in detail in Ulloa et al. [83]. In the present study, the effect of a non-vanishing p, known at this stage, is readily incorporated into the procedure through the constitutive equation (52).

4.5. Spatial discretization

Equations (79), (82), and (83) are discretized using standard finite elements, where the global primary fields $\boldsymbol{u}$, p, and α are interpolated with bilinear shape functions, while the local field $\boldsymbol{\varepsilon}^{\mathrm{p}}$ is evaluated at Gauss integration points. This straightforward procedure is not elaborated here for the sake of brevity.

We remark that the chosen finite elements cannot describe the discontinuities in the function spaces (64) and (67), for which discontinuous finite element techniques should be considered. Nevertheless, it has been shown for ductile phase-field models with perfect plasticity that a strong concentration of plastic strains is attained, representing a regularized version of the discontinuous response, where the element size plays the role of a convergence parameter [122]. This behavior is observed for the proposed model in the dry case [83] and in the numerical simulations presented in section 5 for the present extension to saturated porous media. Note that this remark is only relevant if $p = 0$ in the compressive/shear regime at the limit of $\alpha \to 1$.

5. Numerical simulations

This section is devoted to finite element simulations that highlight the main features of the proposed model. In all examples, plane-strain conditions are assumed, and a low-level initial damage $\alpha_0 = 1 \times 10^{-5}$ is uniformly distributed in the domain to allow for plastic-damage evolution in the compressive/shear regime.

5.1. Homogeneous response

As a prelude to more involved boundary value problems, we first present the homogeneous response of the model, aiming for an illustrative description of the hydromechanical coupling effects. To this end, a single quadrilateral element of unit area is loaded in uniaxial compression by applying monotonic displacements on a single side while keeping the opposite side fixed in the direction of the load. Moreover, undrained conditions are simulated by setting the element sides impermeable, i.e., not fixing the pore pressure.

The following material parameters are selected: Young's modulus $E = 14$ GPa, Poisson's ratio $\nu = 0.31$, and friction coefficient $A_\varphi = 0.401$. A reference dilation coefficient $\bar{A}_\theta = 0.289$ is chosen, and the influence of non-associativity is assessed by varying the dilation coefficient as $A_\theta \in \{\bar{A}_\theta, \bar{A}_\theta/2, 0\}$. In a homogeneous response in the compressive/shear regime, $\operatorname{tr} \boldsymbol{s}^{\mathrm{p}} < 0$ holds at all times; thus, the mode I fracture toughness G_{cI} does not play a role, and the damage behavior is solely modulated by the ratio between the mode II fracture toughness and the length scale, chosen as $G_{\mathrm{cII}}/\ell = 0.581$ N/mm^2, and the fracture degradation parameter, chosen as $b = 10$. Similarly, the permeability parameters play no role in the undrained homogeneous response; the fluid effect is modulated by the Biot coefficient, chosen as $B = 0.9$, and the Biot modulus, varied as $M \in \{100, 500, 1000\}$ MPa in order to study the hydromechanical coupling.

Figure 5 shows the response of the model for the single element test, comparing the results of varying M with the results of the dry case, i.e., with $p = 0$ at all times. We note that significant differences are observed between the dry case and the fluid-saturated cases, exhibiting notable hydromechanical coupling effects. Moreover, these differences strongly depend on the amount of plastic dilation. For $A_\theta = \bar{A}_\theta$,

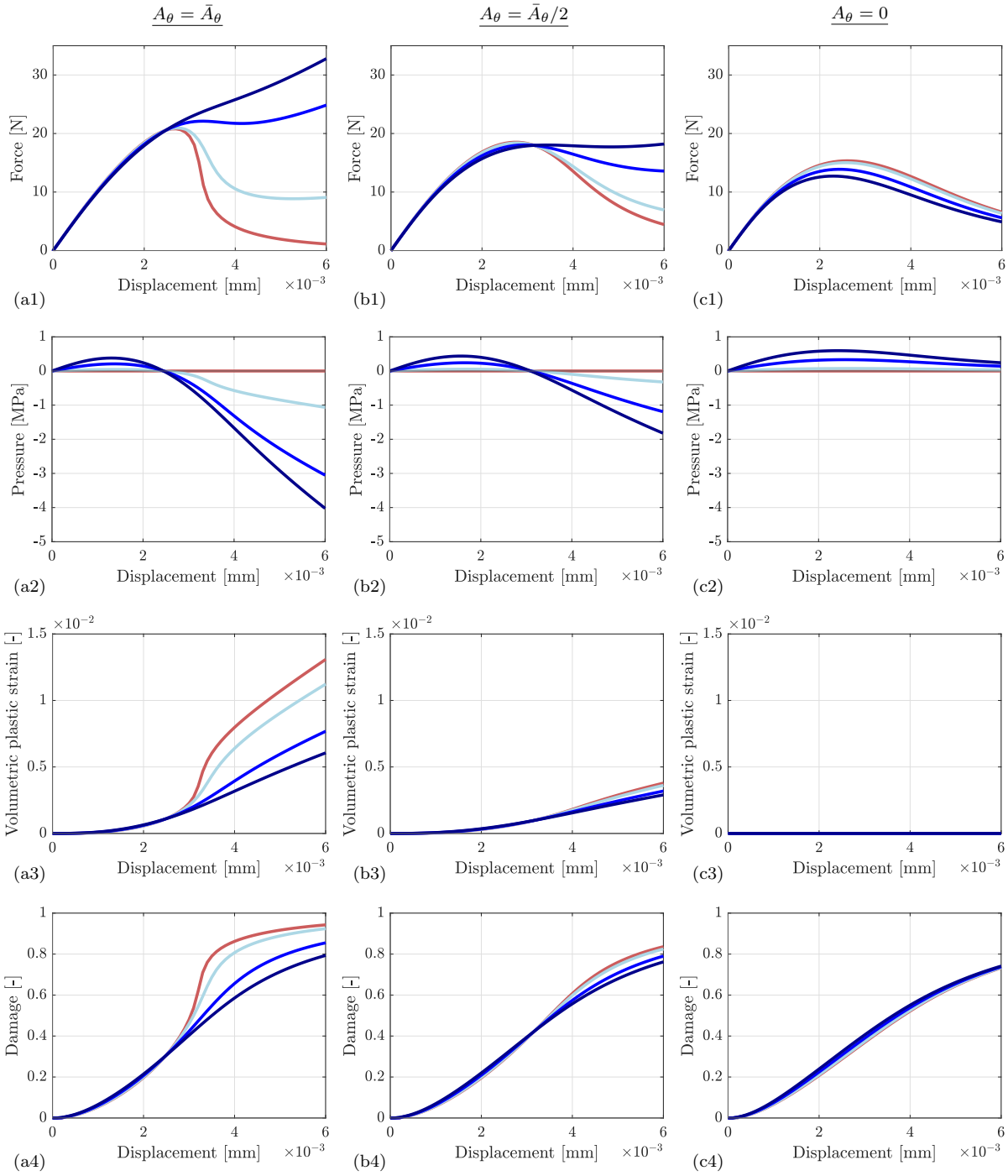

Fig. 5. Imposed displacement vs. (x1) force, (x2) pressure p, (x3) equivalent plastic strain κ, and (x4) damage α for uniaxial compression in the dry case (red) and the saturated case with $M = 100$ MPa (light blue), $M = 500$ MPa (blue), and $M = 1000$ MPa (dark blue). The dilation coefficient is varied as $A_\theta = \bar{A}_\theta$ (ax), $A_\theta = \bar{A}_\theta/2$ (bx), and $A_\theta = 0$ (cx).

figure 5(a) shows that for the dry case, a typical hardening-softening response is observed, modulated by the coupled plastic-damage evolution. On the other hand, the saturated cases with increasing M show enhanced hardening and an apparent increase in strength. This response is due to the evolution of negative pore pressure, which in turn is due to the growth of volumetric plastic strains. This behavior can be further explained from equations (81) and (82), which show that (i) the pressure increment scales linearly with M and (ii) dilatant volumetric strains are related to pressure drops. Thus, an initial contraction causes the pressure to increase, but later, the volumetric plastic strains dominate the response, promoting a cohesive mechanism in the pore space. Clearly, this apparent increase in strength does not reflect the mechanical properties of the solid, since letting the fluid drain at constant displacements would cause the force in figure 5(a1) to drop. Figure 5(b) shows qualitatively similar results for $A_\theta = \bar{A}_\theta/2$, but in this case, the apparent strengthening of the sample is less pronounced as a consequence of lower dilation. Finally, for $A_\theta = 0$, the opposite effect is observed: the absence of plastic dilation results in positive pore pressures, which cause the saturated samples to be weaker than the dry sample. As expected, this weakening is more pronounced as the pressure increases, as achieved by higher M values. The results of this example suggest that the influence of the dilation coefficient is significant in the hydromechanical coupled evolution, and that an overestimation of volumetric plastic strains may lead to an overestimation of hardening effects. Therefore, the non-associative frictional plasticity model employed in this work plays a crucial role in the response.

5.2. Biaxial compression

The second example highlights the ability of the model to describe shear banding and shear fracture in saturated porous media. To this end, we consider a biaxial compression test in a rectangular sample with a central hole (figure 6). A uniform mesh of ∼43000 quadrilateral elements with a characteristic element size

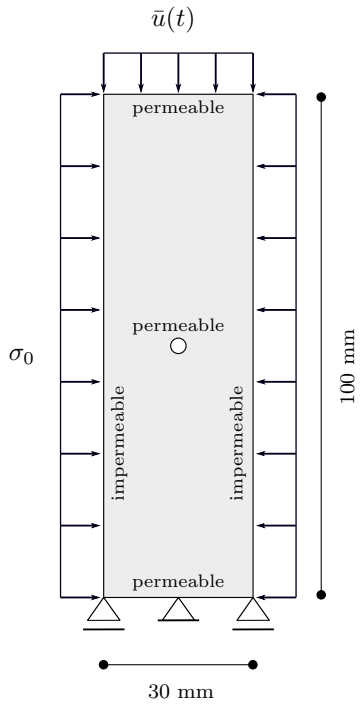

Fig. 6. Schematic representation of the biaxial compression test in a specimen with a central hole of 3.4 mm diameter. The confining stress is fixed at $\sigma_0 = 5$ MPa during the displacement loading stage.

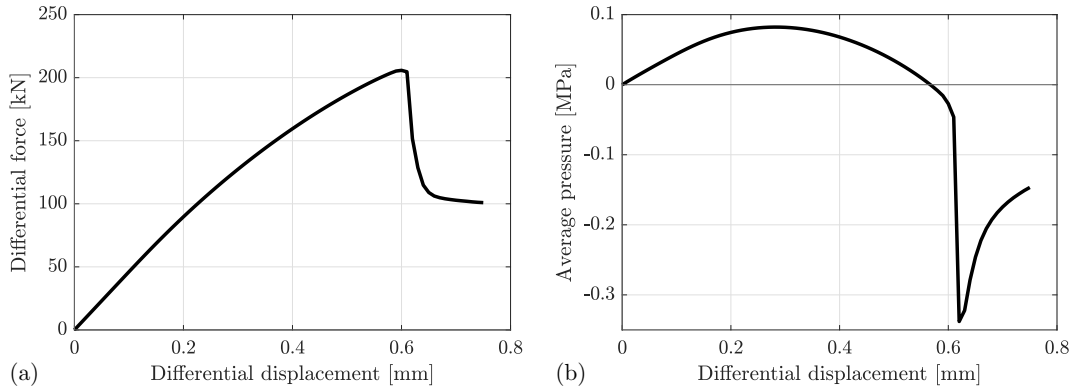

Fig. 7. Imposed vertical displacement vs. (a) force and (b) average pressure p for the biaxial compression test. The specimen has an out-of-plane thickness of 100 mm.

$h_{\mathrm{c}} = 0.3$ mm is employed. The test is divided into two loading stages. In the first stage, confining stress is gradually applied until $\sigma_0 = 5$ MPa, keeping the vertical displacements at the bottom edge fixed, where only the center node is also fixed horizontally. In this loading stage, the specimen is completely drained. For the second loading stage, the lateral confining stress σ_0 is fixed while vertical displacements $\bar{u}$ are imposed downwards in increments of 0.01 mm and time steps $\Delta t = 5 \times 10^{-5}$. Moreover, free fluid flow, i.e., $\bar{p} = 0$, is assumed through the walls of the central hole as well as the top and the bottom edges, while an impermeable boundary is considered for the left and the right sides.

For this example, we select the following material parameters: Young's modulus $E = 14$ GPa, Poisson's ratio $\nu = 0.31$, friction coefficient $A_\varphi = 0.401$, dilation coefficient $A_\theta = 0.289$, mode I fracture toughness $G_{\mathrm{cI}} = 1.033$ N/m, mode II fracture toughness $G_{\mathrm{cII}} = 58.108$ N/m, degradation parameter $b = 25$, length scale $\ell = 0.97$ mm, Biot coefficient $B = 0.9$, Biot modulus $M = 100$ MPa, permeability constant $K_{\mathrm{D}} = 5 \times 10^{-8}$ mm^2, fluid viscosity (for water) $\eta_{\mathrm{vf}} = 1 \times 10^{-9}$ MPa$\cdot$s, and transition exponent $\epsilon = 50$. Finally, the damage viscosity is fixed as $\eta_{\mathrm{vd}} = 2 \times 10^{-9}$ MPa$\cdot$s; this value did not show a noticeable effect in the response and can thus be viewed as a purely numerical artefact.

Figure 7(a) shows the force-displacement curve at the top edge. A peak load is observed at $\bar{u} = 0.61$ mm, followed by a softening stage that ends in a residual strength plateau. Note that here, the residual strength of the solid skeleton is modulated by the friction coefficient and the confining stress, as expected in a sliding failure mode. In particular, figure 8 shows a hydrostatic generalized stress profile at peak load where the tensile region ($\mathrm{tr}\,\boldsymbol{s}^{\mathrm{p}} = 0$, i.e., open microcracks) can be clearly distinguished from the compressive/shear region ($\mathrm{tr}\,\boldsymbol{s}^{\mathrm{p}} < 0$, i.e., closed microcracks with frictional sliding). The equivalent plastic strain and damage profiles hint shear banding before the peak load, with cracks nucleating at the hole. At the post-peak stage, two shear cracks propagate from the hole in (practically) the same direction, where figure 8(b2) shows a strong concentration of plastic strains in a very narrow band, exhibiting a clear mode II fracture process.

Figure 7(b) shows the average pressure in the specimen versus the imposed vertical displacement, while figure 9 shows the pressure profiles at different time steps. When the loading starts, overpressures are generated throughout the specimen, reaching an average peak at $\bar{u} = 0.3$ mm. Subsequently, the pressure drops as a consequence of plastic dilation, particularly in the regions near the hole. At the peak load ($\bar{u} = 0.61$ mm), the pressure profile shows marked regions of negative pressure, coinciding with the regions of plastic strain concentration in figure 8(b1). The physical interpretation of this result is that fluid is strongly drawn towards regions with a significant growth of frictional-dilational microcracks. This is further observed

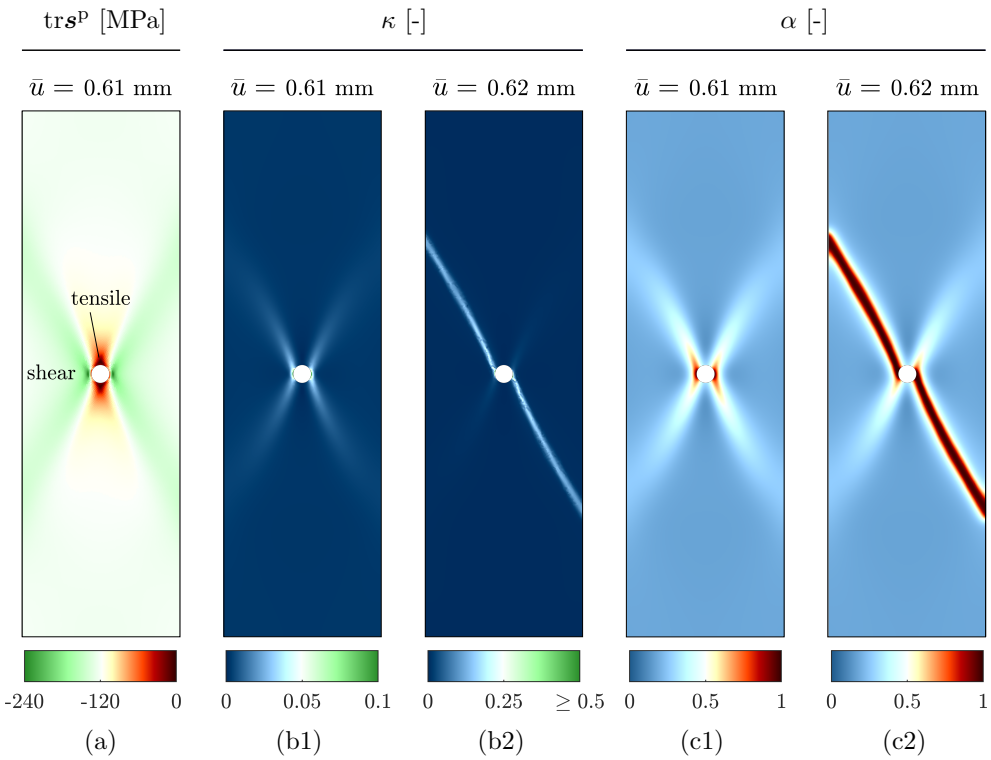

Fig. 8. Shear fracture process in the biaxial compression test for the perforated saturated specimen: (a) pre-failure hydrostatic generalized stress tr $\boldsymbol{s}^{\mathrm{p}}$ [MPa], (b) pre- and post-failure equivalent plastic strain, and (c) pre- and post-failure damage profile.

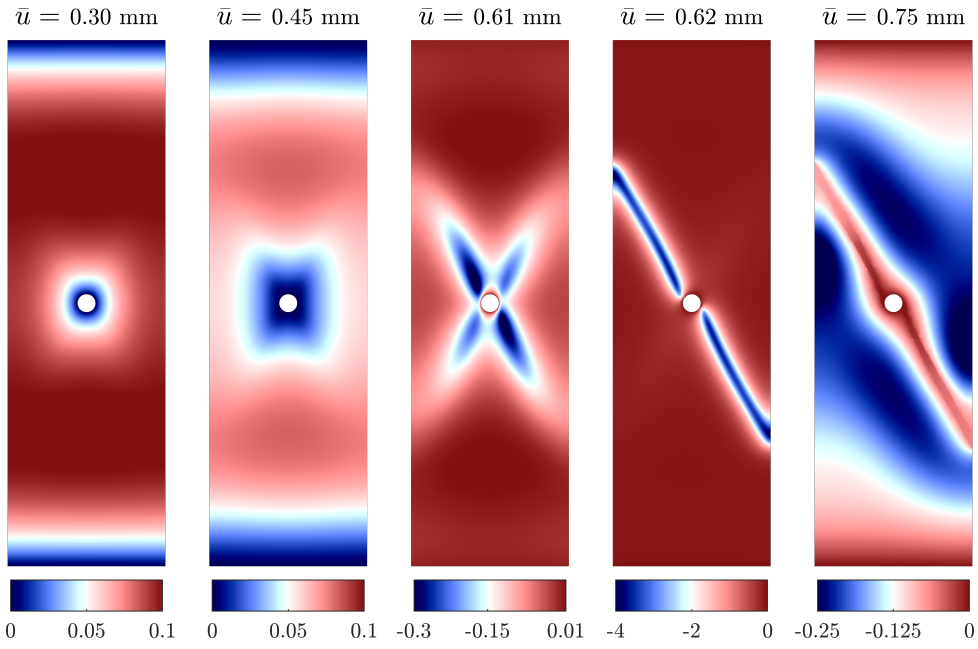

Fig. 9. Evolution of the pore pressure p [MPa] during the shear fracture process in the biaxial compression test.

at $\bar{u} = 0.62$ mm, when the macroscopic shear cracks are fully developed, showing a negative pressure band along the failure plane. We note that qualitatively similar results have been obtained in previous studies employing strong discontinuities [34, 37]. Finally, during the residual plateau, figure 7(b) shows that the negative pressure slowly dissipates. This is further evidenced in figure 9 for $\bar{u} = 0.75$ mm where, due to its enhanced permeability, the macroscopic crack resembles a permeable boundary with vanishing overpressure.

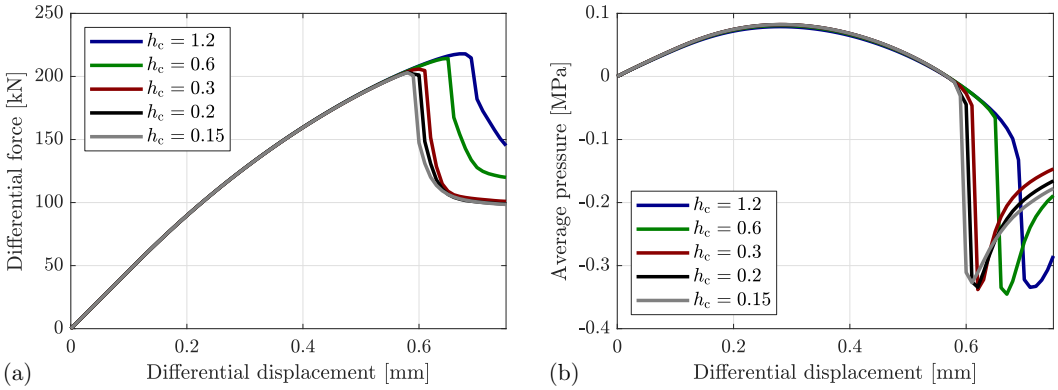

Fig. 10. Biaxial compression test for different mesh sizes h_c [mm], showing the imposed displacement vs. (a) the reaction force and (b) the average pore pressure in the domain.

Finally, figure 10 shows the response for different mesh sizes. The force-displacement curves suggest mesh convergence throughout the entire response, including the post-fracture stage at the residual strength plateau. Similarly, the average pressure shows mesh convergence up to failure; however, the average pressure response suggests a slower, non-monotonic convergence in the post-fracture stage. This result does not reflect upon the novel aspects of the present model but rather on the expected limitations of the heuristic computation of the crack aperture. As previously discussed, more dedicated definitions of the crack aperture [86, 127] can be adopted to improve the mesh convergence, without altering the novel aspects of the model. Nevertheless, it is worth remarking that the model essentially converges to two sliding blocks at the post-fracture stage. Thus, we are mainly concerned with the response of the model up to complete fracture, captured reliably in the present simulation in terms of mesh sensitivity.

5.3. Hydraulic fracturing of a square specimen

The third example considers a benchmark problem for the phase-field modeling of hydraulic fracture [100, 101, 128], consisting of a tensile fracture process driven by fluid volume injection. The boundary value problem in figure 11(a) shows a square plate with a single predefined notch. The domain is discretized using quadrilateral elements of characteristic size $h_c = 0.5$ mm in a wide central region parallel to the axis of the notch. The displacements are fixed in both directions at the boundary, where the pressure is also set to zero. A constant fluid flux $\bar{h} = 0.75$ mm^2/s is injected through the notch for an interval of 2.5 s, discretized in the simulation in time steps $\Delta t = 0.001$ s. Figure 11(b) shows the predefined crack surface modeled by setting $\alpha = 1$ in the corresponding nodes and obtaining the optimal profile, i.e., solving equation (83) with $s^{\mathrm{d}} = 0$. We consider the following material parameters: fracture length scale $\ell = 5h_c = 2.5$ mm, degradation parameter $b = 1$, damage viscosity $\eta_{\mathrm{vd}} = 1 \times 10^{-3}$ MPa$\cdot$s, Biot coefficient $B = 1$, Biot modulus $M = 300$ MPa, and permeability constant $K_{\mathrm{D}} = 1 \times 10^{-10}$ mm^2. All other material parameters are the same as in the previous example.

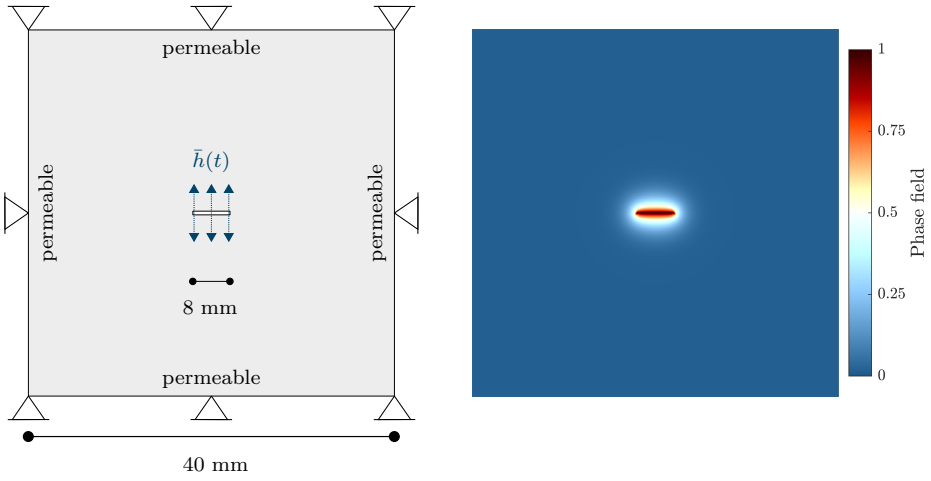

Fig. 11. Schematic representation of the hydraulically induced fracture test on a square specimen (left). A constant flux $\bar{h} = 0.75$ mm^2/s is applied during 2.5 seconds in time steps $\Delta t = 0.001$ s. The initial fracture where the fluid is injected is modeled by setting $\alpha = 1$ along the crack and obtaining the corresponding optimal profile (right).

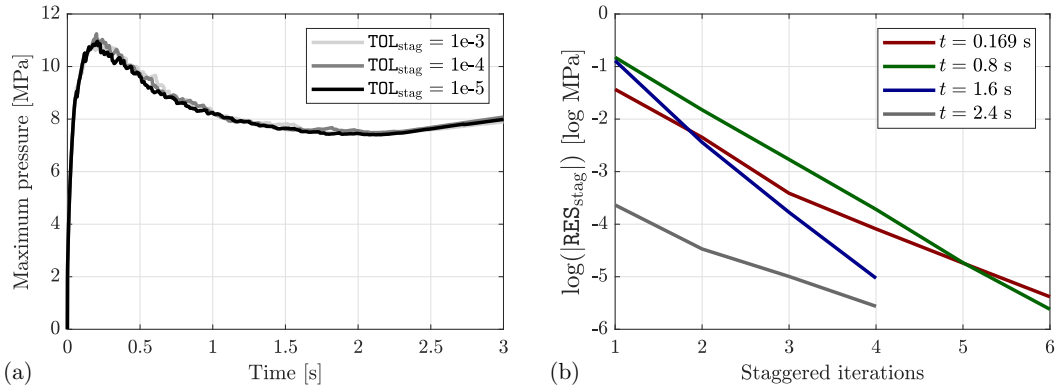

Fig. 12. (a) Time vs. maximum pore pressure in the specimen for different tolerances and (b) convergence of the staggered scheme at different time steps for the stricter tolerance.

We first illustrate in figure 12(a) the evolution of the maximum fluid pressure in the crack region versus the fluid injection time. It is noted that the pressure initially increases up to a peak. Thereafter, as expected from previous studies [88, 100, 101], a drop in fluid pressure is observed. Additionally, in figure 12(a), the maximum pressure versus time is plotted for different tolerance values $\texttt{TOL}_{\text{stag}}$ (see algorithm 1), showing a rather stable behavior. Note that, as reported in the phase-field literature [96, 134], some pressure oscillations are observed along the crack path, resulting from a stepwise pressure build-up–crack propagation process. We also investigate the convergence performance of the algorithm based on the staggered residual, shown in the logarithmic scale for different time steps in figure 12(b). In all cases, at most 6 staggered iterations are required to reach convergence for $\left|\texttt{RES}_{\text{stag}}\right| \leq 1 \times 10^{-5}$.

Figure 13 illustrates the main mechanisms of the proposed model, showing (a) the vertical displacement u_y, (b) the fluid pressure p, (c) the hydrostatic generalized stress $\text{tr}\boldsymbol{s}^{\text{P}}$, and (d) the crack phase-field α at different injection times. At $t = 0.17$ s, the crack begins to grow into the tensile regions at the notch tips due to the fluid-induced pressure build-up. Thereafter, the central crack propagates horizontally in both directions towards the boundary. At all times, figure 13(c) shows a clear tensile region ($\text{tr}\,\boldsymbol{s}^{\text{P}} = 0$,

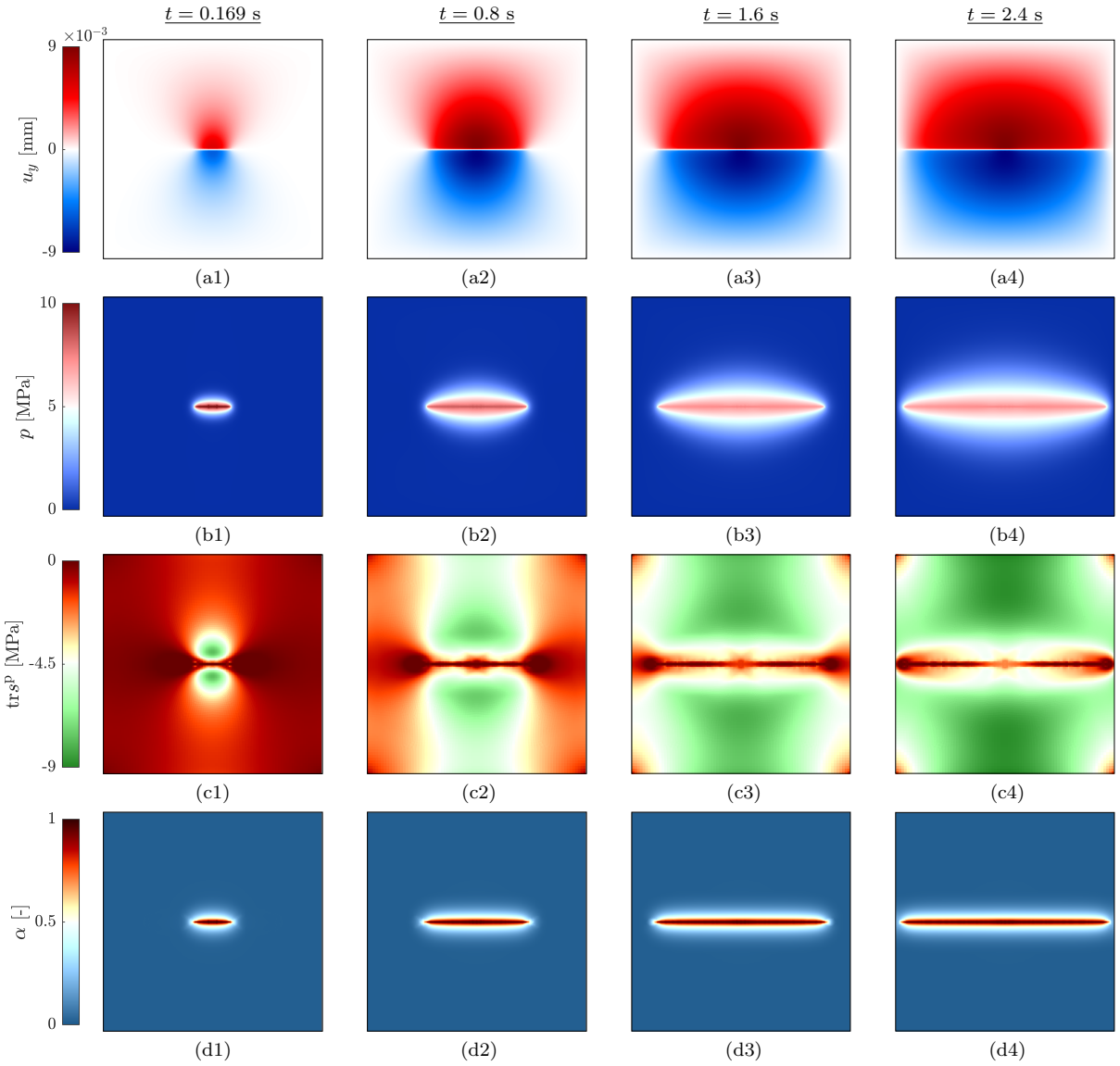

Fig. 13. Hydraulic fracture process in the square specimen at different time steps: (a) vertical displacement component u_y [mm], (b) pore pressure p [MPa], (c) hydrostatic generalized stress $\mathrm{tr}\,\boldsymbol{s}^{\mathrm{p}}$ [MPa], and crack phase-field α.

i.e., open microcracks) ahead of the crack tips, while the material above and below the crack is under compression/shear ($\mathrm{tr}\,\boldsymbol{s}^{\mathrm{p}} < 0$, i.e., closed microcracks with frictional sliding). Thus, the model properly predicts a brittle fracture process, in agreement with the micromechanical considerations. Owing to the permeability enhancement in equation (63), figure 13(b) shows that the fluid readily fills up the crack as it propagates. Therefore, at a given time, the pressure stabilizes and is nearly constant over the length of the crack. As time goes by, the pressure in the fracture drops, as already evidenced in figure 12(a).

6. Conclusions

In this work, a new variational micromechanics-based phase-field model for hydromechanical fracture in fluid-saturated quasi-brittle materials has been presented. The energetics of the model are established

from micromechanical considerations and include (i) a brittle tensile regime associated with mode I fracture, corresponding to the growth of opening microcracks, and (ii) a non-associative ductile compressive/shear regime associated with mode II fracture, corresponding to the growth of closed microcracks subject to frictional sliding. These mechanisms are coupled to a Biot-Darcy-Poisseulle model for fluid flow in fracturing porous media under saturated conditions. Despite the non-associativity, the model is constructed using thermodynamically consistent variational principles that couple the rate-independent dissipative processes of the solid skeleton to the rate-dependent fluid transport process.

The paradigmatic numerical simulations suggest that the model is able to capture relevant hydromechanical coupling effects in fracturing solids, in agreement with previous findings in the literature. However, to our knowledge, the present phase-field model is the first in the literature to be based on a micromechanical description of damage and plasticity in porous media. The benefit is that these processes are endowed with a clear physical meaning and thus require limited phenomenological assumptions. Moreover, both shear and tensile fracture can be captured in a unified manner, under both mechanical and fluid-driven external actions.

Several topics of future research emerge from the present study. The assumption of isotropic behavior can be relaxed by considering crack families with given orientations. For this purpose, the anisotropic version of the micromechanical framework [14] can be taken as a point of departure. Concerning fluid flow, a more dedicated computation of the permeability tensor at fracture can be considered, aiming to resolve the limitations of the adopted estimation of the crack aperture and direction [86, 127]. In this context, bridging the permeability tensor with the micromechanical aspects of the model appears as a worthy task. Additionally, the negative pore pressure related to plastic dilation calls for enhancements of the model to consider, e.g., cavitation effects. Extensions of the model to fatigue are of interest for materials under hydromechanical cyclic loading, as often present in offshore structures. Here, ideas from the phase-field modeling of fatigue in ductile materials [64] may be taken into account. Concerning numerics, the use of alternative strategies, e.g., meshless techniques employed recently in complex multiphysics problems [135, 136], appears as an interesting direction to explore. Finally, experimental verification and further numerical simulations are required for parameter identification. Here, several factors can be considered, for instance, concerning the role of initial damage and/or porosity conditions. For this task, the Bayesian inversion framework developed in recent works [100, 137] suggests a possible starting point.

Appendix

A. Reduced saddle-point formulation

In addition to the variational statements of section 2.5, we may further establish a reduced saddle-point principle in terms of the triplet $\{\dot{\boldsymbol{u}}, \dot{\mathbf{a}}, p\}$. To this end, we introduce a *grand-canonical potential* [112]

$$\psi^{\mathrm{f}\star}(\boldsymbol{\varepsilon}, p, \mathbf{a}, \nabla\mathbf{a}) = \psi\big(\boldsymbol{\varepsilon}, \check{\zeta}(\boldsymbol{\varepsilon}, p, \mathbf{a}, \nabla\mathbf{a}), \mathbf{a}, \nabla\mathbf{a}\big) - p\,\check{\zeta}(\boldsymbol{\varepsilon}, p, \mathbf{a}, \nabla\mathbf{a}), \tag{A.1}$$

which provides the constitutive relations (6) and (7) in terms of p:

$$\check{\boldsymbol{\sigma}} = \frac{\partial \psi^{\mathrm{f}\star}}{\partial \boldsymbol{\varepsilon}}(\boldsymbol{\varepsilon}, p, \mathbf{a}, \nabla\mathbf{a}), \quad \check{\mathbf{s}} = -\delta_{\mathbf{a}}\psi^{\mathrm{f}\star}(\boldsymbol{\varepsilon}, p, \mathbf{a}, \nabla\mathbf{a}), \quad \text{and} \quad \check{\zeta} = -\frac{\partial}{\partial p}\psi^{\mathrm{f}\star}(\boldsymbol{\varepsilon}, p, \mathbf{a}, \nabla\mathbf{a}). \tag{A.2}$$

In this appendix, the notation $\check{\square}$ is employed to denote a dependent state variable as a function of p rather than ζ. Defining the potential energy functional

$$\mathcal{E}^{\mathrm{f}\star}(\boldsymbol{u}, p, \mathbf{a}) = \int_{\Omega} \psi^{\mathrm{f}\star}(\boldsymbol{\varepsilon}, p, \mathbf{a}, \nabla\mathbf{a})\,\mathrm{d}\boldsymbol{x} \tag{A.3}$$

and the *dual* fluid dissipation functional

$$\mathcal{V}^{\star}(p; \boldsymbol{u}, \zeta, \mathbf{a}) = -\int_{\Omega} \phi^{\star}_{\mathrm{con}}(-\nabla p; \mathbf{c})\,\mathrm{d}\boldsymbol{x}, \tag{A.4}$$

the reduced saddle-point principle reads

$$\inf_{\dot{\boldsymbol{u}}\in\dot{\mathscr{U}}} \sup_{p\in\mathscr{P}} \inf_{\dot{\mathbf{a}}\in\dot{\mathscr{A}}} \left\{ \frac{\mathrm{d}}{\mathrm{d}t}\mathcal{E}^{\mathrm{f}\star}(\boldsymbol{u}, p, \mathbf{a}) + \mathcal{V}^{\star}(p; \boldsymbol{u}, \zeta, \mathbf{a}) + \mathcal{R}(\dot{\mathbf{a}}; \boldsymbol{u}, \zeta, \mathbf{a}, \mathbf{s}) - \mathcal{P}^{u}(t, \dot{\boldsymbol{u}}) - \mathcal{P}^{p}(t, p) \right\}. \tag{A.5}$$

This formulation is primal for the solid phase and dual for the fluid phase, in terms of $\{\boldsymbol{u}, \dot{\mathbf{a}}\}$ and p, respectively. The necessary conditions of (A.5) coincide with those of (25), but with the local constitutive relation $(6)_2$ already condensed out. This approach can be viewed as an extended version of the classical $\boldsymbol{u}-p$ formulation in poroelasticity, further accounting for the evolution of gradient-enhanced internal variables.

With the variational principle (A.5) in mind, the grand-canonical potential (A.1) evaluated for the model proposed in section 3.2 takes the form

$$\psi^{\mathrm{f}\star}(\boldsymbol{\varepsilon}, p, \boldsymbol{\varepsilon}^{\mathrm{p}}, \alpha) = \begin{cases} \dfrac{1}{2}\,\boldsymbol{\varepsilon} : \mathbf{C}^{\mathrm{dam}}(\alpha) : \boldsymbol{\varepsilon} - \dfrac{p^2}{2M^{\mathrm{dam}}(\alpha)} - B^{\mathrm{dam}}(\alpha)\, p\,\mathrm{tr}\,\boldsymbol{\varepsilon} & \text{if open,} \\ \dfrac{1}{2}(\boldsymbol{\varepsilon} - \boldsymbol{\varepsilon}^{\mathrm{p}}) : \mathbf{C} : (\boldsymbol{\varepsilon} - \boldsymbol{\varepsilon}^{\mathrm{p}}) + \dfrac{1}{2}\,\boldsymbol{\varepsilon}^{\mathrm{p}} : \mathbf{H}^{\mathrm{kin}}(\alpha) : \boldsymbol{\varepsilon}^{\mathrm{p}} - \dfrac{p^2}{2M} - B\,p\,\mathrm{tr}(\boldsymbol{\varepsilon} - \boldsymbol{\varepsilon}^{\mathrm{p}}) - p\,\mathrm{tr}\,\boldsymbol{\varepsilon}^{\mathrm{p}} & \text{if closed.} \end{cases} \tag{A.6}$$

The constitutive equations (A.2) yield the relations

$$\check{\boldsymbol{\sigma}}(\boldsymbol{\varepsilon}, p, \boldsymbol{\varepsilon}^{\mathrm{p}}, \alpha) = \frac{\partial \psi^{\mathrm{f}\star}}{\partial \boldsymbol{\varepsilon}} = \begin{cases} \mathbf{C}^{\mathrm{dam}}(\alpha) : \boldsymbol{\varepsilon} - B^{\mathrm{dam}}(\alpha)\, p\mathbf{1} & \text{if open,} \\ \mathbf{C} : (\boldsymbol{\varepsilon} - \boldsymbol{\varepsilon}^{\mathrm{p}}) - B\,p\mathbf{1} & \text{if closed,} \end{cases} \tag{A.7}$$

and

$$\check{\zeta}(\boldsymbol{\varepsilon}, p, \boldsymbol{\varepsilon}^{\mathrm{p}}, \alpha) = -\frac{\partial \psi^{\mathrm{f}\star}}{\partial p} = \begin{cases} \dfrac{p}{M^{\mathrm{dam}}(\alpha)} + B^{\mathrm{dam}}(\alpha)\,\mathrm{tr}\,\boldsymbol{\varepsilon} & \text{if open,} \\ \dfrac{p}{M} + B\,\mathrm{tr}(\boldsymbol{\varepsilon} - \boldsymbol{\varepsilon}^{\mathrm{p}}) + \mathrm{tr}\,\boldsymbol{\varepsilon}^{\mathrm{p}} & \text{if closed.} \end{cases} \tag{A.8}$$

Likewise, we obtain the generalized stress conjugate to the plastic strain tensor

$$\check{\boldsymbol{s}}^{\mathrm{p}}(\boldsymbol{\varepsilon}, p, \boldsymbol{\varepsilon}^{\mathrm{p}}, \alpha) = -\frac{\partial \psi^{\mathrm{f}\star}}{\partial \boldsymbol{\varepsilon}^{\mathrm{p}}} = \begin{cases} \boldsymbol{0} & \text{if open,} \\ \boldsymbol{\mathsf{C}} : (\boldsymbol{\varepsilon} - \boldsymbol{\varepsilon}^{\mathrm{p}}) - \boldsymbol{\mathsf{H}}^{\mathrm{kin}}(\alpha) : \boldsymbol{\varepsilon}^{\mathrm{p}} - B\,p\boldsymbol{1} + p\boldsymbol{1} & \text{if closed,} \end{cases} \tag{A.9}$$

and the generalized stress conjugate to the crack phase-field

$$\check{s}^{\mathrm{d}}(\boldsymbol{\varepsilon}, p, \boldsymbol{\varepsilon}^{\mathrm{p}}, \alpha) = -\frac{\partial \psi^{\mathrm{f}\star}}{\partial \alpha} = \begin{cases} -\dfrac{1}{2K}\, g_K'(\alpha)\,(K\,\mathrm{tr}\,\boldsymbol{\varepsilon} - Bp + p)^2 - g_\mu'(\alpha)\,\mu\,\boldsymbol{\varepsilon}_{\mathrm{dev}} : \boldsymbol{\varepsilon}_{\mathrm{dev}} & \text{if open,} \\ -\dfrac{1}{2}\, H_K^{\mathrm{kin}\prime}(\alpha)(\mathrm{tr}\,\boldsymbol{\varepsilon}^{\mathrm{p}})^2 - \dfrac{1}{2}\, H_\mu^{\mathrm{kin}\prime}(\alpha)\,\boldsymbol{\varepsilon}^{\mathrm{p}}_{\mathrm{dev}} : \boldsymbol{\varepsilon}^{\mathrm{p}}_{\mathrm{dev}} & \text{if closed,} \end{cases} \tag{A.10}$$

which are equivalent to the ζ-dependent forms (47) and (52). The saddle-point problem (69) is then replaced by its reduced version in the sense of (A.5), which takes the form

$$\begin{aligned} \inf_{\dot{\boldsymbol{u}} \in \mathscr{U}} \inf_{\dot{\boldsymbol{\varepsilon}}^{\mathrm{p}} \in \mathscr{B}} \inf_{\dot{\alpha} \in \mathscr{D}} \sup_{p \in \mathscr{P}} \Bigg\{ \int_\Omega \Big(\check{\boldsymbol{\sigma}} : \nabla^{\mathrm{s}} \dot{\boldsymbol{u}} - \check{\zeta}\,\dot{p} - \check{\boldsymbol{s}}^{\mathrm{p}} : \dot{\boldsymbol{\varepsilon}}^{\mathrm{p}} - \check{s}^{\mathrm{d}}\,\dot{\alpha} - \frac{1}{2}\boldsymbol{K}(\boldsymbol{\varepsilon}, \alpha, \nabla\alpha) : (\nabla p \otimes \nabla p) \Big)\,\mathrm{d}\boldsymbol{x} - \mathcal{P}^p(t, p) \\ + \int_\Omega \Big(\frac{\mathrm{tr}\,\dot{\boldsymbol{\varepsilon}}^{\mathrm{p}}}{3A_\theta}(A_\theta - A_\varphi)\,\mathrm{tr}\,\boldsymbol{s}^{\mathrm{p}} + \frac{G_{\mathrm{c}}(\boldsymbol{s}^{\mathrm{p}})}{\ell}\big(\alpha\,\dot{\alpha} + \ell^2 \nabla\alpha \cdot \nabla\dot{\alpha}\big) \Big)\mathrm{d}\boldsymbol{x} - \mathcal{P}^u(t, \dot{\boldsymbol{u}}) \Bigg\}, \end{aligned} \tag{A.11}$$

with $\check{\boldsymbol{\sigma}}$, $\check{\boldsymbol{s}}^{\mathrm{p}}$, $\check{s}^{\mathrm{d}}$, and $\check{\zeta}$ given as functions of $\boldsymbol{u}$, p, $\boldsymbol{\varepsilon}^{\mathrm{p}}$, and α in equations (A.7), (A.8), (A.9), and (A.10). The mechanical balance, the plasticity evolution equations, and the damage evolution equations directly follow from (A.11) in the same way as in section 3.2.3, albeit with the stress and the driving forces in terms of p. On the other hand, taking variations of the objective functional in (A.11) with respect to p yields

$$\int_\Omega \left[\frac{\partial}{\partial p}\Big(\check{\boldsymbol{\sigma}} : \nabla^{\mathrm{s}} \dot{\boldsymbol{u}} - \check{\zeta}\,\dot{p} - \check{\boldsymbol{s}}^{\mathrm{p}} : \dot{\boldsymbol{\varepsilon}}^{\mathrm{p}} - \check{s}^{\mathrm{d}}\,\dot{\alpha} \Big)\tilde{p} - \nabla p \cdot \boldsymbol{K}(\boldsymbol{\varepsilon}, \alpha, \nabla\alpha) \cdot \nabla\tilde{p} \right] \mathrm{d}\boldsymbol{x} - \int_{\Gamma_{\mathrm{N}}^p} \bar{h}\,\tilde{p}\,\mathrm{d}S = 0 \quad \forall\,\tilde{p} \in \tilde{\mathscr{P}}. \tag{A.12}$$

In the first term, we readily identify the negative rate of fluid content variation:

$$\frac{\partial}{\partial p}\Big(\check{\boldsymbol{\sigma}} : \nabla^{\mathrm{s}} \dot{\boldsymbol{u}} - \check{\zeta}\,\dot{p} - \check{\boldsymbol{s}}^{\mathrm{p}} : \dot{\boldsymbol{\varepsilon}}^{\mathrm{p}} - \check{s}^{\mathrm{d}}\,\dot{\alpha} \Big) = \frac{\partial}{\partial p}\left(\frac{\mathrm{d}}{\mathrm{d}t} \psi^{\mathrm{f}\star}(\boldsymbol{\varepsilon}, p, \boldsymbol{\varepsilon}^{\mathrm{p}}, \alpha) \right) = \frac{\mathrm{d}}{\mathrm{d}t}\left(\frac{\partial}{\partial p} \psi^{\mathrm{f}\star}(\boldsymbol{\varepsilon}, p, \boldsymbol{\varepsilon}^{\mathrm{p}}, \alpha) \right) = -\dot{\zeta}\,. \tag{A.13}$$

Thus, equation (A.12) represents the weak form of the fluid balance equations (2).

Acknowledgements

F. Aldakheel and N. Noii were funded by the Priority Program DFG-SPP 2020 within its second funding phase.

References

[1] L. Dormieux, D. Kondo, and F.-J. Ulm. *Microporomechanics*. John Wiley & Sons, 2006.

[2] F. Aldakheel. A microscale model for concrete failure in poro-elasto-plastic media. *Theoretical and Applied Fracture Mechanics*, 107:102517, 2020.

[3] P.A. Vermeer and R. de Borst. Non-associated plasticity for soils, concrete and rock. *HERON, 29 (3), 1-64*, 1984.

[4] J. Lubliner, J. Oliver, S. Oller, and E. Oñate. A plastic-damage model for concrete. *International Journal of Solids and Structures*, 25(3):299–326, 1989.

[5] C. Chazallon and P.Y. Hicher. A constitutive model coupling elastoplasticity and damage for cohesive-frictional materials. *Mechanics of Cohesive-frictional Materials*, 3(1):41–63, 1998.

[6] A.-S. Chiarelli, J.-F. Shao, and N. Hoteit. Modeling of elastoplastic damage behavior of a claystone. *International Journal of Plasticity*, 19(1):23–45, 2003.

[7] M.R. Salari, S. Saeb, K.J. Willam, S.J. Patchet, and R.C. Carrasco. A coupled elastoplastic damage model for geomaterials. *Computer Methods in Applied Mechanics and Engineering*, 193(27-29):2625–2643, 2004.

[8] J.Y. Wu, J. Li, and R. Faria. An energy release rate-based plastic-damage model for concrete. *International Journal of Solids and Structures*, 43(3-4):583–612, 2006.

[9] F. Parisio, S. Samat, and L. Laloui. Constitutive analysis of shale: a coupled damage plasticity approach. *International Journal of Solids and Structures*, 75:88–98, 2015.

[10] E. Lanoye, F. Cormery, D. Kondo, and J.-F. Shao. An isotropic unilateral damage model coupled with frictional sliding for quasi-brittle materials. *Mechanics Research Communications*, 53:31–35, 2013.

[11] J.-J. Marigo and K. Kazymyrenko. A micromechanical inspired model for the coupled to damage elasto-plastic behavior of geomaterials under compression. *Mechanics & Industry*, 20(1):105, 2019.

[12] S. Andrieux, Y. Bamberger, and J.-J. Marigo. Un modèle de matériau microfissuré pour les bétons et les roches. *Journal of Theoretical and Applied Mechanics*, 5(3):471–513, 1986.

[13] V. Pensée, D. Kondo, and L. Dormieux. Micromechanical analysis of anisotropic damage in brittle materials. *Journal of Engineering Mechanics*, 128(8):889–897, 2002.

[14] Q.-Z. Zhu, D. Kondo, and J.-F. Shao. Micromechanical analysis of coupling between anisotropic damage and friction in quasi brittle materials: role of the homogenization scheme. *International Journal of Solids and Structures*, 45(5):1385–1405, 2008.

[15] Q.-Z. Zhu, J.-F. Shao, and D. Kondo. A micromechanics-based thermodynamic formulation of isotropic damage with unilateral and friction effects. *European Journal of Mechanics-A/Solids*, 30(3):316–325, 2011.

[16] L.-Y. Zhao, Q.-Z. Zhu, and J.-F. Shao. A micro-mechanics based plastic damage model for quasi-brittle materials under a large range of compressive stress. *International Journal of Plasticity*, 100:156–176, 2018.

[17] C. Jia, Q. Zhang, and S. Wang. Experimental investigation and micromechanical modeling of elastoplastic damage behavior of sandstone. *Materials*, 13(15):3414, 2020.

[18] J.-F. Shao, Y. Jia, D. Kondo, and A.-S. Chiarelli. A coupled elastoplastic damage model for semi-brittle materials and extension to unsaturated conditions. *Mechanics of Materials*, 38(3):218–232, 2006.

[19] Y. Jia, X.C. Song, G. Duveau, K. Su, and J.-F. Shao. Elastoplastic damage modelling of argillite in partially saturated condition and application. *Physics and Chemistry of the Earth, Parts A/B/C*, 32(8-14):656–666, 2007.

[20] F. Parisio and L. Laloui. Plastic-damage modeling of saturated quasi-brittle shales. *International Journal of Rock Mechanics and Mining Sciences*, 93:295–306, 2017.

[21] D.-W. Hu, H. Zhou, and J.-F. Shao. An anisotropic damage–plasticity model for saturated quasi-brittle materials. *International Journal for Numerical and Analytical Methods in Geomechanics*, 37(12):1691–1710, 2013.

[22] L. Dormieux, D. Kondo, and F.-J. Ulm. A micromechanical analysis of damage propagation in fluid-saturated cracked media. *Comptes Rendus Mecanique*, 334(7):440–446, 2006.

[23] N. Xie, Q.-Z. Zhu, J.-F. Shao, and L.-H. Xu. Micromechanical analysis of damage in saturated quasi brittle materials. *International Journal of Solids and Structures*, 49(6):919–928, 2012.

[24] C. Jia, S. Zhang, and W. Xu. Experimental investigation and numerical modeling of coupled elastoplastic damage and permeability of saturated hard rock. *Rock Mechanics and Rock Engineering*, 54(3):1151–1169, 2021.

[25] M.A. Biot. General theory of three-dimensional consolidation. *Journal of Applied Physics*, 12(2):155–164, 1941.

[26] O. Coussy. *Mechanics of porous continua*. Wiley, 1995.

[27] A. Needleman. Non-normality and bifurcation in plane strain tension and compression. *Journal of the Mechanics and Physics of Solids*, 27(3):231–254, 1979.

[28] S.A. Sabet and R. de Borst. Structural softening, mesh dependence, and regularisation in non-associated plastic flow. *International Journal for Numerical and Analytical Methods in Geomechanics*, 43(13):2170–2183, 2019.

[29] J. Oliver, M. Cervera, and O. Manzoli. Strong discontinuities and continuum plasticity models: the strong discontinuity approach. *International Journal of Plasticity*, 15(3):319–351, 1999.

[30] R.A. Regueiro and R.I. Borja. Plane strain finite element analysis of pressure sensitive plasticity with strong discontinuity. *International Journal of Solids and Structures*, 38(21):3647–3672, 2001.

[31] Q. Chen, J.E. Andrade, and E. Samaniego. AES for multiscale localization modeling in granular media. *Computer Methods in Applied Mechanics and Engineering*, 200(33):2473–2482, 2011.

[32] L.-Y. Zhao, J.-F. Shao, and Q.-Z. Zhu. Analysis of localized cracking in quasi-brittle materials with a micromechanics based friction-damage approach. *Journal of the Mechanics and Physics of Solids*, 119:163–187, 2018.

[33] J. Larsson and R. Larsson. Finite-element analysis of localization of deformation and fluid pressure in an elastoplastic porous medium. *International Journal of Solids and Structures*, 37(48-50):7231–7257, 2000.

[34] C. Callari and F. Armero. Finite element methods for the analysis of strong discontinuities in coupled poroplastic media. *Computer Methods in Applied Mechanics and Engineering*, 191(39-40):4371–4400, 2002.

[35] A.R. Khoei, M. Vahab, E. Haghighat, and S. Moallemi. A mesh-independent finite element formulation for modeling crack growth in saturated porous media based on an enriched-FEM technique. *International Journal of Fracture*, 188(1):79–108, 2014.

[36] E. Mikaeili and B. Schrefler. XFEM, strong discontinuities and second-order work in shear band modeling of saturated porous media. *Acta Geotechnica*, 13(6):1249–1264, 2018.

[37] E. Hadzalic, A. Ibrahimbegovic, and M. Nikolic. Failure mechanisms in coupled poro-plastic medium. *Coupled Systems Mechanics*, 7:43–59, 2018.

[38] M. Nikolic, A. Ibrahimbegovic, and P. Miscevic. Discrete element model for the analysis of fluid-saturated fractured poro-plastic medium based on sharp crack representation with embedded strong discontinuities. *Computer Methods in Applied Mechanics and Engineering*, 298:407–427, 2016.

[39] F. Oka, T. Adachi, and A. Yashima. A strain localization analysis using a viscoplastic softening model for clay. *International Journal of Plasticity*, 11(5):523–545, 1995.

[40] M. Cervera, J. Oliver, and O. Manzoli. A rate-dependent isotropic damage model for the seismic analysis of concrete dams. *Earthquake engineering & structural dynamics*, 25(9):987–1010, 1996.

[41] H.-B. Mühlhaus and I. Vardoulakis. The thickness of shear bands in granular materials. *Geotechnique*, 37(3): 271–283, 1987.

[42] R. de Borst and L.J. Sluys. Localisation in a Cosserat continuum under static and dynamic loading conditions. *Computer Methods in Applied Mechanics and Engineering*, 90(1-3):805–827, 1991.

[43] Z.P. Bažant and M. Jirásek. Nonlocal integral formulations of plasticity and damage: survey of progress. *Journal of Engineering Mechanics*, 128(11):1119–1149, 2002.

[44] M. Jirásek. Non-local damage mechanics with application to concrete. *Revue française de Génie Civil*, 8(5-6): 683–707, 2004.

[45] P. Grassl and M. Jirásek. Plastic model with non-local damage applied to concrete. *International Journal for Numerical and Analytical Methods in Geomechanics*, 30(1):71–90, 2006.

[46] R.H.J. Peerlings, R. de Borst, W.A.M. Brekelmans, and M.G.D. Geers. Gradient-enhanced damage modelling of concrete fracture. *Mechanics of Cohesive-frictional Materials*, 3(4):323–342, 1998.

[47] J. Pamin, H. Askes, and R. de Borst. Two gradient plasticity theories discretized with the element-free Galerkin method. *Computer Methods in Applied Mechanics and Engineering*, 192(20-21):2377–2403, 2003.

[48] I. Zreid and M. Kaliske. A gradient enhanced plasticity–damage microplane model for concrete. *Computational Mechanics*, 62(5):1239–1257, 2018.

[49] R. de Borst and T. Duretz. On viscoplastic regularisation of strain-softening rocks and soils. *International Journal for Numerical and Analytical Methods in Geomechanics*, 44(6):890–903, 2020.

[50] T. Hageman, S.A. Sabet, and R. de Borst. Convergence in non-associated plasticity and fracture propagation for standard, rate-dependent, and Cosserat continua. *International Journal for Numerical Methods in Engineering*, 122(3):777–795, 2021.

[51] H.W. Zhang and B.A. Schrefler. Gradient-dependent plasticity model and dynamic strain localisation analysis of saturated and partially saturated porous media: one dimensional model. *European Journal of Mechanics-A/Solids*, 19(3):503–524, 2000.

[52] W. Ehlers and W. Volk. On theoretical and numerical methods in the theory of porous media based on polar and non-polar elasto-plastic solid materials. *International Journal of Solids and Structures*, 35(34-35):4597–4617, 1998.

[53] F. Collin, R. Chambon, and R. Charlier. A finite element method for poro mechanical modelling of geotechnical problems using local second gradient models. *International Journal for Numerical Methods in Engineering*, 65 (11):1749–1772, 2006.

[54] K. Yoshioka, F. Parisio, D. Naumov, R. Lu, O. Kolditz, and T. Nagel. Comparative verification of discrete and smeared numerical approaches for the simulation of hydraulic fracturing. *GEM-International Journal on Geomathematics*, 10(1):13, 2019.

[55] G.A. Francfort and J.-J. Marigo. Revisiting brittle fracture as an energy minimization problem. *Journal of the Mechanics and Physics of Solids*, 46(8):1319–1342, 1998.

[56] B. Bourdin, G.A. Francfort, and J.-J. Marigo. Numerical experiments in revisited brittle fracture. *Journal of the Mechanics and Physics of Solids*, 48(4):797–826, 2000.

[57] H. Amor, J.-J. Marigo, and C. Maurini. Regularized formulation of the variational brittle fracture with unilateral contact: Numerical experiments. *Journal of the Mechanics and Physics of Solids*, 57(8):1209–1229, 2009.

[58] C. Miehe, M. Hofacker, and F. Welschinger. A phase field model for rate-independent crack propagation: Robust algorithmic implementation based on operator splits. *Computer Methods in Applied Mechanics and Engineering*, 199(45):2765–2778, 2010.

[59] K. Pham, H. Amor, J.-J. Marigo, and C. Maurini. Gradient damage models and their use to approximate brittle fracture. *International Journal of Damage Mechanics*, 20(4):618–652, 2011.

[60] M.J. Borden, C.V. Verhoosel, M.A. Scott, T.J.R. Hughes, and C.M. Landis. A phase-field description of dynamic brittle fracture. *Computer Methods in Applied Mechanics and Engineering*, 217:77–95, 2012.

[61] C. Kuhn, A. Schlüter, and R. Müller. On degradation functions in phase field fracture models. *Computational Materials Science*, 108:374–384, 2015.

[62] K. Weinberg and C. Hesch. A high-order finite deformation phase-field approach to fracture. *Continuum Mechanics and Thermodynamics*, 29(4):935–945, 2017.

[63] A.C. Hansen-Dörr, F. Dammaß, R. de Borst, and M. Kästner. Phase-field modeling of crack branching and deflection in heterogeneous media. *Engineering Fracture Mechanics*, 232:107004, 2020.

[64] J. Ulloa, J. Wambacq, R. Alessi, G. Degrande, and S. François. Phase-field modeling of fatigue coupled to cyclic plasticity in an energetic formulation. *Computer Methods in Applied Mechanics and Engineering*, 373: 113473, 2021.

[65] P.K. Kristensen, C.F. Niordson, and E. Martínez-Pañeda. An assessment of phase field fracture: crack initiation and growth. *Philosophical Transactions of the Royal Society A*, 379(2203):20210021, 2021.

[66] N.P. van Dijk, J.J. Espadas-Escalante, and P. Isaksson. Strain energy density decompositions in phase-field fracture theories for orthotropy and anisotropy. *International Journal of Solids and Structures*, 196:140–153, 2020.

[67] F. Freddi and G. Royer-Carfagni. Regularized variational theories of fracture: a unified approach. *Journal of the Mechanics and Physics of Solids*, 58(8):1154–1174, 2010.

[68] L. De Lorenzis and C. Maurini. Nucleation under multi-axial loading in variational phase-field models of brittle fracture. *International Journal of Fracture*, May 2021.

[69] M. Ambati, T. Gerasimov, and L. De Lorenzis. A review on phase-field models of brittle fracture and a new fast hybrid formulation. *Computational Mechanics*, 55(2):383–405, 2015.

[70] J.Y. Wu and V.P. Nguyen. A length scale insensitive phase-field damage model for brittle fracture. *Journal of the Mechanics and Physics of Solids*, 119:20–42, 2018.

[71] A. Kumar, B. Bourdin, G.A. Francfort, and O. Lopez-Pamies. Revisiting nucleation in the phase-field approach to brittle fracture. *Journal of the Mechanics and Physics of Solids*, page 104027, 2020.

[72] B. Shen and O. Stephansson. Modification of the G-criterion for crack propagation subjected to compression. *Engineering Fracture Mechanics*, 47(2):177–189, 1994.

[73] J.M. Ramsey and F.M. Chester. Hybrid fracture and the transition from extension fracture to shear fracture. *Nature*, 428(6978):63–66, 2004.

[74] G. Lancioni and G. Royer-Carfagni. The variational approach to fracture mechanics. a practical application to the French Panthéon in Paris. *Journal of Elasticity*, 95(1-2):1–30, 2009.

[75] X. Zhang, S.W. Sloan, C. Vignes, and D. Sheng. A modification of the phase-field model for mixed mode crack propagation in rock-like materials. *Computer Methods in Applied Mechanics and Engineering*, 322:123–136, 2017.

[76] A. Spetz, R. Denzer, E. Tudisco, and O. Dahlblom. Phase-field fracture modelling of crack nucleation and propagation in porous rock. *International Journal of Fracture*, 224(1):31–46, 2020.

[77] E.C. Bryant and W. Sun. A mixed-mode phase field fracture model in anisotropic rocks with consistent kinematics. *Computer Methods in Applied Mechanics and Engineering*, 342:561–584, 2018.

[78] F. Fei and J. Choo. Double-phase-field formulation for mixed-mode fracture in rocks. *Computer Methods in Applied Mechanics and Engineering*, 376:113655, 2021.

[79] J. Choo and W. Sun. Coupled phase-field and plasticity modeling of geological materials: From brittle fracture to ductile flow. *Computer Methods in Applied Mechanics and Engineering*, 330:1–32, 2018.

[80] D. Kienle, F. Aldakheel, and M.-A. Keip. A finite-strain phase-field approach to ductile failure of frictional materials. *International Journal of Solids and Structures*, 172:147–162, 2019.

[81] T. You, H. Waisman, and Q.-Z. Zhu. Brittle-ductile failure transition in geomaterials modeled by a modified phase-field method with a varying damage-driving energy coefficient. *International Journal of Plasticity*, 136: 102836, 2021.

[82] E.C. Bryant and W. Sun. Phase field modeling of frictional slip with slip weakening/strengthening under non-isothermal conditions. *Computer Methods in Applied Mechanics and Engineering*, 375:113557, 2021.

[83] J. Ulloa, J. Wambacq, R. Alessi, E. Samaniego, G. Degrande, and S. François. A micromechanics-based variational phase-field model for fracture in geomaterials with brittle-tensile and compressive-ductile behavior. *Journal of the Mechanics and Physics of Solids*, 159:104684, 2022.

[84] T. You, H. Waisman, W.-Z. Chen, J.-F. Shao, and Q.-Z. Zhu. A novel micromechanics-enhanced phase-field model for frictional damage and fracture of quasi-brittle geomaterials. *Computer Methods in Applied Mechanics and Engineering*, 385:114060, 2021.

[85] A. Mikelić, M.F. Wheeler, and T. Wick. A phase-field method for propagating fluid-filled fractures coupled to a surrounding porous medium. *SIAM Multiscale Model. Simul.*, 13(1):367–398, 2015.

[86] Z.A. Wilson and C.M. Landis. Phase-field modeling of hydraulic fracture. *Journal of the Mechanics and Physics of Solids*, 96:264–290, 2016.

[87] Y. Heider and B. Markert. A phase-field modeling approach of hydraulic fracture in saturated porous media. *Mechanics Research Communications*, 80:38–46, 2017.

[88] S. Lee, M.F. Wheeler, and T. Wick. Pressure and fluid-driven fracture propagation in porous media using an adaptive finite element phase field model. *Computer Methods in Applied Mechanics and Engineering*, 305: 111–132, 2016.

[89] W. Ehlers and C. Luo. A phase-field approach embedded in the theory of porous media for the description of dynamic hydraulic fracturing. *Computer methods in applied mechanics and engineering*, 315:348–368, 2017.

[90] D. Santillán, R. Juanes, and L. Cueto-Felgueroso. Phase field model of fluid-driven fracture in elastic media: Immersed-fracture formulation and validation with analytical solutions. *Journal of Geophysical Research: Solid Earth*, 122(4):2565–2589, 2017.

[91] T. Cajuhi, L. Sanavia, and L. De Lorenzis. Phase-field modeling of fracture in variably saturated porous media. *Computational Mechanics*, 61(3):299–318, 2018.

[92] S. Zhou, X. Zhuang, and T. Rabczuk. Phase field method for quasi-static hydro-fracture in porous media under stress boundary condition considering the effect of initial stress field. *Theoretical and Applied Fracture Mechanics*, 107:102523, 2020.

[93] C. Chukwudozie, B. Bourdin, and K. Yoshioka. A variational phase-field model for hydraulic fracturing in porous media. *Computer Methods in Applied Mechanics and Engineering*, 347:957–982, 2019.

[94] Y. Heider and W. Sun. A phase field framework for capillary-induced fracture in unsaturated porous media: Drying-induced vs. hydraulic cracking. *Computer Methods in Applied Mechanics and Engineering*, 359:112647, 2020.

[95] C. Miehe and S. Mauthe. Phase field modeling of fracture in multi-physics problems. Part III. Crack driving forces in hydro-poro-elasticity and hydraulic fracturing of fluid-saturated porous media. *Computer Methods in Applied Mechanics and Engineering*, 304:619–655, 2016.

[96] Y. Heider. A review on phase-field modeling of hydraulic fracturing. *Engineering Fracture Mechanics*, 253: 107881, 2021.

[97] T. Wick. *Multiphysics phase-field fracture: modeling, adaptive discretizations, and solvers*, volume 28. Walter de Gruyter GmbH & Co KG, 2020.

[98] S. Mauthe and C. Miehe. Hydraulic fracture in poro-hydro-elastic media. *Mechanics Research Communications*, 80:69–83, 2017.

[99] L. Xia, J. Yvonnet, and S. Ghabezloo. Phase field modeling of hydraulic fracturing with interfacial damage in highly heterogeneous fluid-saturated porous media. *Engineering Fracture Mechanics*, 186:158–180, 2017.

[100] N. Noii, A. Khodadadian, and T. Wick. Bayesian inversion for anisotropic hydraulic phase-field fracture. *Computer Methods in Applied Mechanics and Engineering*, 386:114118, 2021.

[101] F. Aldakheel, N. Noii, T. Wick, and P. Wriggers. A global–local approach for hydraulic phase-field fracture in poroelastic media. *Computers & Mathematics with Applications*, 91:99–121, 2021.

[102] M. Pise, J. Bluhm, and J. Schröder. Elasto-plastic phase-field model of hydraulic fracture in saturated binary porous media. *International Journal for Multiscale Computational Engineering*, 17(2), 2019.

[103] D. Kienle and M.-A. Keip. A variational minimization formulation for hydraulically induced fracturing in elastic-plastic solids. *International Journal of Fracture*, pages 1–25, 2021.

[104] A. Mielke and T. Roubícek. *Rate-Independent systems. Theory and application.* Springer, 2015.

[105] J. Ulloa, R. Alessi, J. Wambacq, G. Degrande, and S. François. On the variational modeling of non-associative plasticity. *International Journal of Solids and Structures*, 217:272–296, 2021.

[106] C. Miehe. A multi-field incremental variational framework for gradient-extended standard dissipative solids. *Journal of the Mechanics and Physics of Solids*, 59(4):898–923, 2011.

[107] C. Miehe, S. Mauthe, and S. Teichtmeister. Minimization principles for the coupled problem of Darcy–Biot-type fluid transport in porous media linked to phase field modeling of fracture. *Journal of the Mechanics and Physics of Solids*, 82:186–217, 2015.

[108] B. Halphen and Q.S. Nguyen. Generalized standard materials. *Journal de Mécanique*, 14(1):39–63, 1975.

[109] O. Coussy. *Poromechanics*. John Wiley & Sons, 2004.

[110] G.A. Francfort. Recovering convexity in non-associated plasticity. *Comptes Rendus Mécanique*, 346(3):198–205, 2018.

[111] C. Miehe, S. Mauthe, and H. Ulmer. Formulation and numerical exploitation of mixed variational principles for coupled problems of Cahn–Hilliard-type and standard diffusion in elastic solids. *International Journal for Numerical Methods in Engineering*, 99(10):737–762, 2014.

[112] L. Anand. 2014 Drucker Medal Paper: A derivation of the theory of linear poroelasticity from chemoelasticity. *Journal of Applied Mechanics*, 82(11):111005, 2015.

[113] B. Bourdin, G.A. Francfort, and J.-J. Marigo. The variational approach to fracture. *Journal of Elasticity*, 91 (1-3):5–148, 2008.

[114] R. Alessi and K. Pham. Variational formulation and stability analysis of a three dimensional superelastic model for shape memory alloys. *Journal of the Mechanics and Physics of Solids*, 87:150–176, 2016.

[115] P. Rodríguez, J. Ulloa, C. Samaniego, and E. Samaniego. A variational approach to the phase field modeling of brittle and ductile fracture. *International Journal of Mechanical Sciences*, 144:502–517, 2018.

[116] J.-J. Marigo, C. Maurini, and K. Pham. An overview of the modelling of fracture by gradient damage models. *Meccanica*, 51(12):3107–3128, 2016.

[117] M. Luege, A. Orlando, M.E. Almenar, and E.A. Pilotta. An energetic formulation of a gradient damage model for concrete and its numerical implementation. *International Journal of Solids and Structures*, 155:160–184, 2018.

[118] C. Miehe, S. Teichtmeister, and F. Aldakheel. Phase-field modelling of ductile fracture: a variational gradient-extended plasticity-damage theory and its micromorphic regularization. *Philosophical Transactions of the Royal Society A: Mathematical, Physical and Engineering Science*, 374(2066):20150170, 2016.

[119] L. Böger, M.-A. Keip, and C. Miehe. Minimization and saddle-point principles for the phase-field modeling of fracture in hydrogels. *Computational Materials Science*, 138:474–485, 2017.

[120] R. Jänicke, B. Quintal, F. Larsson, and K. Runesson. Identification of viscoelastic properties from numerical model reduction of pressure diffusion in fluid-saturated porous rock with fractures. *Computational Mechanics*, 63(1):49–67, 2019.

[121] T. Mori and K. Tanaka. Average stress in matrix and average elastic energy of materials with misfitting inclusions. *Acta Metallurgica*, 21(5):571–574, 1973.

[122] R. Alessi, J.-J. Marigo, and S. Vidoli. Gradient damage models coupled with plasticity: variational formulation and main properties. *Mechanics of Materials*, 80:351–367, 2015.

[123] Y. Zhao and R.I. Borja. A continuum framework for coupled solid deformation–fluid flow through anisotropic elastoplastic porous media. *Computer Methods in Applied Mechanics and Engineering*, 369:113225, 2020.

[124] I. Vardoulakis. Shear band inclination and shear modulus of sand in biaxial tests. *International Journal for Numerical and Analytical Methods in Geomechanics*, 4(2):103–119, 1980.

[125] P. Laborde. Analysis of the strain-stress relation in plasticity with non-associated laws. *International Journal of Engineering Science*, 25(6):655–666, 1987.

[126] S. Rezaei, J.R. Mianroodi, T. Brepols, and S. Reese. Direction-dependent fracture in solids: Atomistically calibrated phase-field and cohesive zone model. *Journal of the Mechanics and Physics of Solids*, 147:104253, 2021.

[127] K. Yoshioka, D. Naumov, and O. Kolditz. On crack opening computation in variational phase-field models for fracture. *Computer Methods in Applied Mechanics and Engineering*, 369:113210, 2020.

[128] S. Lee, M.F. Wheeler, and T. Wick. Iterative coupling of flow, geomechanics and adaptive phase-field fracture including level-set crack width approaches. *Journal of Computational and Applied Mathematics*, 314:40–60, 2017.

[129] V. Crismale. Energetic solutions for the coupling of associative plasticity with damage in geomaterials. *arXiv preprint arXiv:2109.08450*, 2021.

[130] S. Dana and M.F. Wheeler. Convergence analysis of fixed stress split iterative scheme for anisotropic poroelasticity with tensor Biot parameter. *Computational Geosciences*, 22(5):1219–1230, 2018.

[131] J.C. Simo and T.J.R. Hughes. *Computational inelasticity*. Springer, 1998.

[132] E.A. de Souza Neto, D. Peric, and D.R.J. Owen. *Computational methods for plasticity: theory and applications*. John Wiley & Sons, 2011.

[133] R.I. Borja. *Plasticity: modeling & computation*. Springer Science & Business Media, 2013.

[134] P. Wriggers, F. Aldakheel, L. Lohaus, and M. Heist. Water-induced damage mechanisms of cyclically loaded high-performance concretes. *Bauingenieur*, 95(4):126–132, 2020.

[135] V. Mohammadi and M. Dehghan. Simulation of the phase field Cahn–Hilliard and tumor growth models via a numerical scheme: element-free Galerkin method. *Computer Methods in Applied Mechanics and Engineering*, 345:919–950, 2019.

[136] M. Abbaszadeh, M. Bayat, M. Dehghan, and M.I. Azis. Investigation of generalized Couette hydromagnetic flow of two-step exothermic chemical reaction in a channel via the direct meshless local Petrov–Galerkin method. *Engineering Analysis with Boundary Elements*, 125:178–189, 2021.

[137] N. Noii, A. Khodadadian, J. Ulloa, F. Aldakheel, T. Wick, S. Francois, and P. Wriggers. Bayesian inversion for unified ductile phase-field fracture. *Computational Mechanics*, 68:943–980, 2021.